



# Polyoxometalate Complexes of Anatase-Titanium Dioxide Cores in Water\*\*

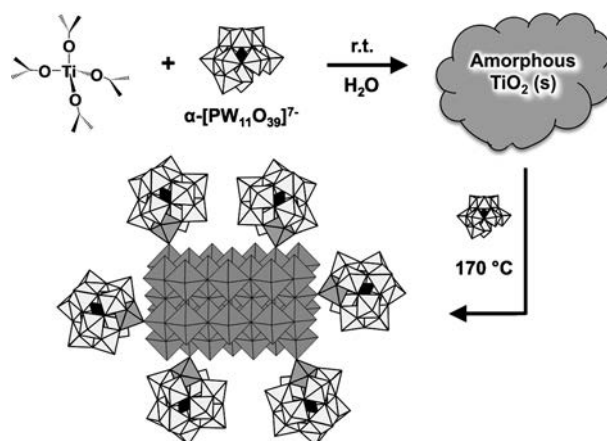
Manoj Raula, Gal Gan Or, Marina Saganovich, Offer Zeiri, Yifeng Wang, Michele R. Chierotti, Roberto Gobetto, and Ira A. Weinstock\*

**Abstract:** Polyoxometalate (POM) cluster anions are shown to serve as covalently coordinated ligands for anatase-TiO<sub>2</sub> nanocrystals, giving isolable assemblies uniquely positioned between molecular macroanions and traditional colloidal nanoparticles. Na<sup>+</sup> salts of the water-soluble polyanionic structures are obtained by reacting amorphous TiO<sub>2</sub> with the 1 nm lacunary ion, Na<sub>7</sub>[α-XW<sub>11</sub>O<sub>39</sub>] (X = P<sup>5+</sup>), at 170 °C, after which an average of 55 α-PW<sub>11</sub>O<sub>39</sub><sup>7-</sup> clusters are found as pentadentate ligands for Ti<sup>IV</sup> ions covalently linked to 6 nm single-crystal anatase cores. The attached POMs are reversible electron acceptors, the reduction potentials of which shift in a predictable fashion by changing the central heteroatom, X, directly influencing a model catalytic reaction. Just as POM cluster anions control the reactivities of metal centers in molecular complexes, directly coordinated POM ligands with tunable redox potentials now provide new options for rationally controlling the reactions of semiconductor nanocrystals.

Polyoxometalates<sup>[1]</sup> (POMs) serve as oxygen-donor ligands for mono-, di-, tri-, and small-nuclearity oxide- and hydroxide-linked fragments of reactive transition (d-block) and main-group (p-block) metal ions, providing molecular complexes that catalyze a variety of oxidative and other processes. In many cases, catalytic activity emerges from the unique properties of the cluster anions, often derivatives of plenary Keggin or Well–Dawson structures, that serve as ligands for the reactive metal centers. This is true as well for POM complexes of Ti<sup>IV</sup> ions,<sup>[2]</sup> some of which catalyze photochemical reductions of CO<sub>2</sub> to methane,<sup>[3]</sup> and selective oxidations by H<sub>2</sub>O<sub>2</sub>.<sup>[4]</sup>

Structurally, a general feature of oxophilic Ti<sup>IV</sup> centers in molecular complexes is their natural tendency to form high-nuclearity oxide-bridged cores. Reported examples include POM complexes, such as [(α-Ti<sub>3</sub>SiW<sub>9</sub>O<sub>37</sub>OH)<sub>3</sub>(TiO<sub>3</sub>-(OH)<sub>2</sub>)<sub>3</sub>]<sup>17-</sup><sup>[2d]</sup> and [(α-1,2,3-P<sub>2</sub>W<sub>15</sub>Ti<sub>3</sub>O<sub>62</sub>)<sub>4</sub>{μ<sub>3</sub>-Ti(OH)<sub>3</sub>Cl}<sub>4</sub>]<sup>45-</sup>,<sup>[5]</sup> with cores of 10 and 16 Ti<sup>IV</sup> atoms, respectively, while up to 34 Ti atoms<sup>[6]</sup> are found in molecular titanium oxide clusters capped by alkoxide and other<sup>[7]</sup> organic anions. Notably, ligand-capped titanium oxide clusters are fundamentally important molecular models for TiO<sub>2</sub> semiconductors.<sup>[6,7]</sup>

We now report a conceptually new role for POM cluster anions as covalently coordinated redox-active ligands in polyanionic complexes of TiO<sub>2</sub>-semiconductor nanocrystals themselves (Scheme 1). Multiple lines of evidence from solid-



**Scheme 1.** Direct coordination of Ti<sup>IV</sup>-substituted POM cluster anions to anatase-TiO<sub>2</sub> cores. The reaction of amorphous TiO<sub>2</sub>(s) (upper right) with the mono-defect Keggin anion, α-PW<sub>11</sub>O<sub>39</sub><sup>7-</sup> (1; white: W<sup>VI</sup>-centered polyhedra; black: P<sup>IV</sup>-centered tetrahedra), gives a clear solution of 6 nm anatase-TiO<sub>2</sub> cores solubilized by covalently attached POM capping ligands, [α-PW<sub>11</sub>O<sub>39</sub>Ti]O<sup>-</sup> (Ti<sup>IV</sup>-centered polyhedra are in gray).

and solution-state analytical methods unequivocally demonstrate that numerous Ti<sup>IV</sup>-substituted mono-defect Keggin-ion capping ligands, [α-PW<sub>11</sub>O<sub>39</sub>Ti]O<sup>-</sup>, are covalently attached to ca. 6 nm anatase-TiO<sub>2</sub> cores (each comprised of 1800 ± 550 Ti atoms), resulting in isolable, water-soluble nanostructures uniquely positioned between molecular macroanions<sup>[2a,5]</sup> and more traditional, electrostatically stabilized, colloidal metal oxides.<sup>[8]</sup> Moreover, the covalently attached POMs serve as tunable electron acceptors at the surfaces of the anatase-semiconductor cores.<sup>[7,9]</sup>

[\*] Dr. M. Raula, G. Gan Or, M. Saganovich, Dr. O. Zeiri, Prof. I. A. Weinstock  
Department of Chemistry, Ben Gurion University of the Negev and the Ilse Katz Institute for Nanoscale Science & Technology  
Beer Sheva, 84105 (Israel)  
E-mail: iraw@bgu.ac.il  
Homepage: <http://www.bgu.ac.il/~iraw>

Prof. Y. Wang  
School of Chemistry and Chemical Engineering  
Shandong University, Ji'nan 250100 (China)

Dr. M. R. Chierotti, Prof. R. Gobetto  
Department of Chemistry and NIS Centre  
University of Turin, Via P. Giuria n° 7, Torino, 10125 (Italy)

[\*\*] I.A.W. thanks the Israel Science Foundation (ISF; 190/13), the ISF & Planning and Budgeting Committee (I-CORE Program 152/11), and the Adelis Foundation, and M.R. thanks the PBC for a Fellowship.

Supporting information for this article is available on the WWW under <http://dx.doi.org/10.1002/anie.201501941>.

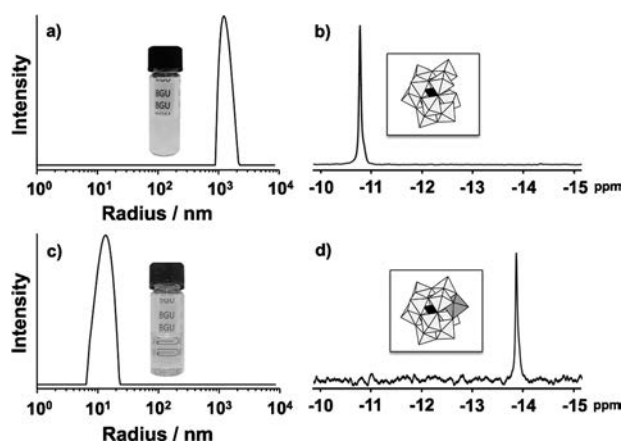


**Figure 1.** Dynamic light scattering (DLS) data (a, c) and  $^{31}\text{P}$  NMR spectra (b, d) before (a, b) and after (c, d) reaction of amorphous  $\text{TiO}_2(\text{s})$  with  $\text{Na}_7[\alpha\text{-PW}_{11}\text{O}_{39}]$  ( $\text{Na}_7\text{1}$ ). Room-temperature hydrolysis of TTIP (8 mM), in the presence of **1** (4 mM), gives micrometer-sized particles of  $\text{TiO}_2(\text{s})$  (a and inset) and no change in the  $^{31}\text{P}$  NMR spectrum of **1** ( $-10.8$  ppm; b). Heating for 20 h at  $170^\circ\text{C}$  gives a clear solution of nano-scale particles (c and inset) and  $[\alpha\text{-PTiW}_{11}\text{O}_{40}]^{5-}$  (**2**) is the only POM observed by  $^{31}\text{P}$  NMR spectroscopy ( $-13.9$  ppm; d). The full  $^{31}\text{P}$  NMR spectrum and a balanced equation are provided in the Supporting Information.

When titanium tetraisopropoxide (TTIP; 8 mM) is added at room temperature to one-half an equivalent of aqueous  $\text{Na}_7[\alpha\text{-PW}_{11}\text{O}_{39}]$  ( $\text{Na}_7\text{1}$ ; 4 mM, pH 6), rapid hydrolysis of the TTIP gives a cloudy solution containing micrometer-sized particles of amorphous  $\text{TiO}_2(\text{s})$  (Figure 1a). The pH remains unchanged,<sup>[10]</sup> as does the  $^{31}\text{P}$  NMR spectrum of **1** (Figure 1b). After 20 h at  $170^\circ\text{C}$ , however, a clear pH 6.5 solution of nanosized particles is obtained (Figure 1c), and  $\alpha\text{-PTiW}_{11}\text{O}_{40}^{5-}$  (**2**),<sup>[4e,f,11]</sup> a byproduct of the reaction, is the only POM observed by  $^{31}\text{P}$  NMR spectroscopy (Figure 1d).

The nanosized  $\text{TiO}_2$ -based particles differ dramatically from traditional examples of electrostatically stabilized colloidal  $\text{TiO}_2$ . They are indefinitely stable in water over a wide range of pH values (from 2 to 8), giving optically clear solutions in the complete absence of added organic ligands.<sup>[12]</sup> Even more remarkable is that, like molecular macroanions, they are uniquely resistant to aggregation: after isolation as solids, they can be stored as water-soluble sodium salts.

Isolation and purification were carried out as follows. First, isopropanol and inorganic byproducts (including **2**) were partially removed from the clear reaction mixture (10 mL) by extensive dialysis against pure water. The dialyzed reaction mixture was then made 2 M in NaCl, giving a cloudy solution from which a hydrated white solid was obtained by centrifugation. When 10 mL of pure water was added, the white solid readily dissolved, once again giving a clear solution. The precipitation/redissolution cycle was carried out four times, reducing the amount of free  $\alpha\text{-PTiW}_{11}\text{O}_{40}^{5-}$  (**2**) to less than 1 pM (based on a dilution factor of ca.  $1 \times 10^{10}$ ). The final white solid readily dissolved in water, with the number-weighted average radius having increased by less than 1 nm (by DLS; Supporting Information, Figure S2), and no change in zeta potential (particle charge), which remained constant at  $-50$  mV.

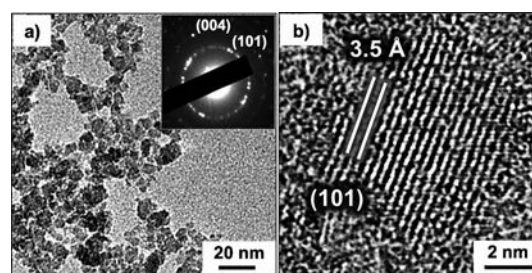


**Figure 2.** Characterization of anatase- $\text{TiO}_2$  nanocrystal cores. a) TEM image of the purified nanoparticles (dried); inset: selected-area electron diffraction pattern of the particles. b) HRTEM image of a single anatase core with fringes corresponding to (101) planes of Ti atoms.

The  $\text{TiO}_2$  cores were characterized by transmission electron microscopy (TEM) and electron and powder X-ray diffraction (XRD). TEM images of dried samples (Figure 2a) revealed an average particle size of  $6.9 \pm 1.4$  nm (based on measurements of 50 particles). Although not morphologically homogeneous, many particles appear to be approximately rectangular prismatic in shape (see the Supporting Information, Figure S3 for more images). Electron diffraction of the particles (inset) featured well-defined rings, indicative of crystalline structure, which when indexed gave a precise match for anatase.<sup>[13,14]</sup>

Debye-Scherrer<sup>[15]</sup> analysis of XRD data (Supporting Information, Figure S3) gave an anatase-crystallite size of  $6.1 \pm 0.2$  nm, statistically identical to the average particle size obtained from TEM images. This correspondence between crystallite size (from XRD) and particle size (from TEM) shows that, on average, each metal oxide core is a single nanocrystal of anatase  $\text{TiO}_2$ .<sup>[14]</sup> Finally, high-resolution TEM (HRTEM) images of the nanocrystals (NCs) revealed exposed facets with atomic fringes separated by distances matching the d-spacing of the (101) planes of anatase (Figure 2b).<sup>[13c]</sup>

Next, capping ligands on the surfaces of the anatase NCs were observed by cryogenic TEM (cryo-TEM) and high-angle annular dark field (HAADF) imaging. Cryo-TEM images (Figure 3a)<sup>[16]</sup> revealed numerous circa 1 nm diameter clus-

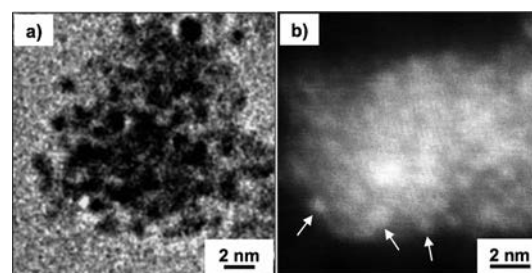


**Figure 3.** Tungsten-based capping ligands on individual anatase- $\text{TiO}_2$  cores. a) Cryo-TEM image of numerous ca. 1 nm clusters (dark objects) on the surface of an anatase NC (for comparison, images of anatase with no surface-attached clusters are provided in the Supporting Information, Figure S4). b) High-angle annular dark field (HAADF) image of the ca. 1 nm clusters on an anatase NC. EDX data (Supporting Information, Figure S5), showed that the numerous bright-white spots (three of which are indicated by arrows) are tungsten based, while the gray areas are mostly titanium.

ters at the surfaces of the anatase cores (see the Supporting Information, Figure S4 for additional images). To our knowledge, this is the first reported image of capping ligands on a soluble metal oxide nanocrystal. The 1 nm clusters were further analyzed by HAADF imaging of a dried sample (Figure 3b), which again revealed numerous circa 1 nm objects, now appearing as white objects on a darker background. Consistent with heavier elements giving rise to brighter regions in HAADF images, data from energy-dispersive X-ray (EDX) spectroscopy (0.4 nm<sup>2</sup> spot analysis) showed the 1 nm objects to be tungsten-based (Supporting Information, Figure S5).

The large abundance of tungsten-based clusters made it possible to obtain a definitive vibrational spectrum of these capping ligands (Figure 4). After correcting the background

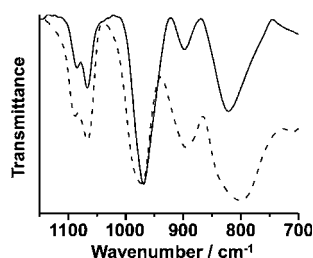


**Figure 4.** Spectroscopic characterization of the heteropolytungstate capping ligands. FTIR spectra of (—): the heteropolytungstate-capped anatase (corrected for absorbance by TiO<sub>2</sub>), and (----): pure Na<sub>5</sub>[α-PTiW<sub>11</sub>O<sub>40</sub>] (Na<sub>5</sub>2).

for absorbance by anatase (Supporting Information, Figure S6), the solid-state FTIR spectrum of the purified material (—) was strikingly similar to that of α-PTi<sup>IV</sup>W<sub>11</sub>O<sub>40</sub><sup>5-</sup> (**2**, ----).

Both featured two P–O stretching bands, at 1066 and 1085 cm<sup>-1</sup>, which are diagnostic for derivatives of the mono-defect ion, α-PW<sub>11</sub>O<sub>39</sub><sup>7-</sup> (**1**), whose central PO<sub>4</sub> units possess local C<sub>3v</sub> symmetry. The 20 cm<sup>-1</sup> separation between these two bands is much smaller however than the circa 40 cm<sup>-1</sup> separation observed for **1** (1085 and 1041 cm<sup>-1</sup>), and unambiguously signifies in-pocket occupancy of the defect site by a metal cation, that is, M<sup>n+</sup> in [α-PM<sup>n+</sup>W<sub>11</sub>O<sub>39</sub>]<sup>(7-n)-</sup>.<sup>[17]</sup> In the present case, M<sup>n+</sup> can only be Ti<sup>IV</sup>. The terminal W=O stretch (at 970 cm<sup>-1</sup>) is also characteristic of M<sup>n+</sup>-substituted ions; in the parent ion, **1**, this band occurs at a much lower energy (950 cm<sup>-1</sup>). Particularly striking is that in both spectra the band at 1066 cm<sup>-1</sup> is more intense than is that at 1085 cm<sup>-1</sup>, a signature that is characteristic of **2**.

The P<sup>V</sup> heteroatom was quantified by X-ray photoelectron spectroscopy (XPS), which analyzes the particle surfaces to a depth of several nm. It gave integrated signal intensities for P 2p and W 4d in an atomic ratio of 1 P per 12 ± 2 W, which is statistically identical to the 1:11 ratio in **2**.<sup>[18]</sup> The presence of P<sup>V</sup> was further confirmed by solid-state <sup>31</sup>P NMR spectroscopy (for the complete solid-state NMR analysis, see the Supporting Information and Figure S7).

The POM capping ligand was independently identified by electrospray ionization mass spectroscopy (ESI-MS). For this,

concentrated HCl was used to dissolve the TiO<sub>2</sub> cores (2 h at 90°C), giving a clear solution of Ti<sup>IV</sup> ions<sup>[19]</sup> and liberated POM-capping ligands.<sup>[20]</sup> Tetrabutylammonium bromide (TBABr) was then added to selectively precipitate the POM as the corresponding TBA salt. After collection of the solid by centrifugation and dissolution in MeCN, ESI-MS revealed {TBA<sub>5</sub>H[PTiW<sub>11</sub>O<sub>40</sub>]}<sup>+</sup>, with an envelope centered at 3953.59, which is nearly identical to the simulated value of 3953.61 (Figure 5; see the Supporting Information, Figure S8 for additional MS data).

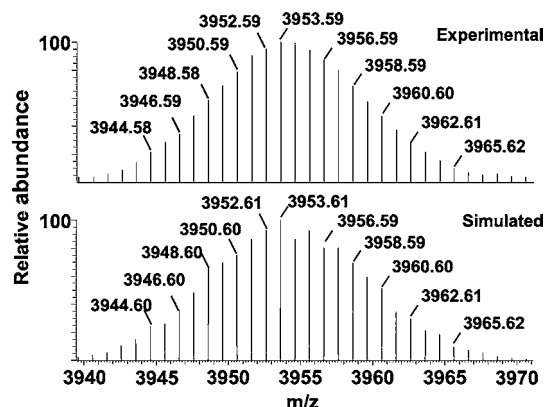


**Figure 5.** ESI mass spectra for the  $z = +1$  ion, {TBA<sub>5</sub>HP[PTiW<sub>11</sub>O<sub>40</sub>]}<sup>+</sup>, a mixed TBA/H<sup>+</sup> salt of [PTiW<sub>11</sub>O<sub>40</sub>]<sup>5-</sup> (**2**). The instrument accuracy is ± 0.1 amu.

Extensive coverage of the anatase surfaces by Ti<sup>IV</sup>-substituted Keggin ions closely related to **2** was supported by wide-area EDX analysis of the bulk material, which gave an atom-percent composition of 25 ± 3 % W to 75 ± 3 % Ti (Supporting Information, Figure S9). Notably, these values correspond to the percentages obtained by simple calculation. If each cluster anion is allocated a reasonable<sup>[21]</sup> 1.8 nm<sup>2</sup> footprint on the anatase surface, an average of 55 ± 10 undecatungstate-based clusters (600 ± 110 W atoms) are present on each ca. 6 nm (1800 ± 550 Ti-atom) anatase core (Supporting Information, Table S1). The zeta potential of the NCs, -50 mV, assigns a net charge of 15e for each assembly,<sup>[22]</sup> such that, like POM monolayers on gold nanoparticles,<sup>[23]</sup> most of the (hydrated) Na<sup>+</sup> counteranions must lie between the closely separated cluster anions.

Although closely related to [α-PTi<sup>IV</sup>W<sub>11</sub>O<sub>40</sub>]<sup>5-</sup> (**2**), the POM capping ligands (heretofore designated **2'**) are directly coordinated to the anatase NCs. This was supported by seven lines of evidence: 1) No aggregation of the NCs was observed by DLS after 14 days of dialysis against pure water (Supporting Information, Figure S2). The pH was nearly identical to the isoelectric point of anatase (pH 6.7), at which its colloids typically precipitate from water.<sup>[24]</sup> If the **2'** cluster anions were electrostatically associated with the TiO<sub>2</sub> NCs, the POM anions would be inherently labile, such that extensive dialysis would eventually remove them from the NC surface, leaving unprotected particles that would certainly precipitate at near-neutral pH. In the present case, however, the solution remained optically clear. Thus, unlike traditional colloids



with electrostatically associated stabilizing ions, the **2'** cluster anions are not labile. 2) After repeated cycles of precipitation (in 2 M NaCl), centrifugation and redissolution, the isolated NCs readily dissolve in pure water to give clear solutions. This is in stark contrast to the insoluble solids obtained when traditional colloids are similarly treated. 3) Upon drying, the POM ligands remain tightly bound to the TiO<sub>2</sub> NCs, giving HAADF images of intact structures (Figure 3b), closely resembling those imaged in their vitrified solution-like state by cryo-TEM (Figure 3a). 4) The repeated NaCl treatments had no effect on the net charges of the nanoparticles: zeta-potential values remained unchanged (−50 mV). 5) The solubility of the NCs in water increased twenty-fold (from 5 to 100 mM Ti) when the Na<sup>+</sup> counter cations were replaced by Li<sup>+</sup>, while 6) replacement of Na<sup>+</sup> by organic counter cations, (*n*Bu<sub>4</sub>N<sup>+</sup> and *n*-Octyl<sub>4</sub>N<sup>+</sup>), gave organic-solvent-soluble analogues: After adding (*n*Bu)<sub>4</sub>NBr to precipitate the **2'**-capped NCs from water, the resultant white solid readily dissolved in MeOH, giving a clear solution (see the Supporting Information, Figure S10 for DLS and TEM data). Analogous *n*-Octyl<sub>4</sub>N<sup>+</sup> salts dissolved in toluene, CH<sub>2</sub>Cl<sub>2</sub>, MeCN, and THF. 7) In a final definitive experiment, no anion-exchange was observed when **2'**-capped anatase NCs were reacted with [α-AlW<sub>12</sub>O<sub>40</sub>]<sup>5−</sup> (1 mM; ca. 600 times the concentration of the NCs, and 10 times that of surface-bound **2'** ligands; Supporting Information, Figure S11).<sup>[25]</sup> None of these findings is compatible with electrostatic association of POMs to the anatase NCs; they can only be understood as the result of a unique situation in which **2'** capping ligands are directly coordinated (covalently attached) to the anatase surface.

This conclusion goes hand-in-hand with the partial consumption of amorphous TiO<sub>2</sub>(s) by **1** during synthesis (Scheme 1), and with the tendency for Ti<sup>IV</sup> ions to form stable oxo-bridged structures. Namely, at 170 °C, **1** initially consumes TiO<sub>2</sub>(s) by serving as a pentadentate ligand for the titanyl ion, Ti=O<sup>2+</sup>, giving freely solvated **2** (Figure 1d). At completion of the reaction, however, numerous POM-ligated Ti<sup>IV</sup> atoms must remain coordinated to the anatase surface. Consistent with this, the Ti=O ligand in **2** readily forms μ-O linkages to other Ti<sup>IV</sup> ions as, for example,<sup>[11]</sup> in [(α-PW<sub>11</sub>O<sub>39</sub>Ti)<sub>2</sub>−μ<sub>2</sub>-O]<sup>8−</sup>. Based on this, and by analogy to alkoxide (RO<sup>−</sup>) ligands on molecular TiO<sub>2</sub> clusters,<sup>[6]</sup> 1 nm [α-PW<sub>11</sub>O<sub>39</sub>Ti]−O<sup>−</sup> capping groups might be coordinated to the anatase surface via [α-PW<sub>11</sub>O<sub>39</sub>Ti]−μ<sub>2</sub>-O<sup>−</sup> linkages to single Ti atoms (upper right in Figure 6a), or via [α-PW<sub>11</sub>O<sub>39</sub>Ti]−μ<sub>3</sub>-O<sup>−</sup> linkages to two Ti atoms (left in Figure 6a). Further studies will address this issue, which might only be resolved by single-crystal X-ray diffraction of molecular analogues with smaller TiO<sub>2</sub> cores.<sup>[26]</sup>

Meanwhile, unlike simple alkoxide capping ligands, **2'** is redox active, serving as a well-behaved electron acceptor.<sup>[27]</sup> This was demonstrated using a 1.7 μM solution of **2'**-capped anatase NCs in 200 mM LiClO<sub>4</sub> (Figure 6b; Supporting Information, Figure S13). Differential pulse voltammetry (DPV; a technique much more sensitive than cyclic voltammetry) gave definitive cathodic currents with maxima at ca. −565 and −790 mV, followed by corresponding anodic currents, indicating that the capping ligands are cleanly reduced and re-oxidized on the anatase surface.<sup>[28]</sup>

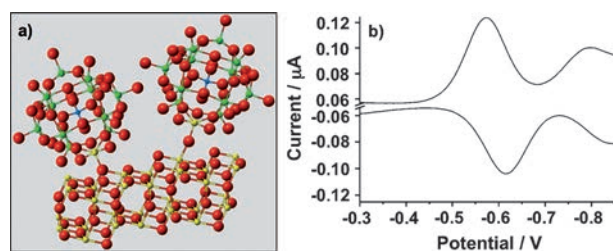


**Figure 6.** Coordination modes and redox chemistry of POM capping ligands on anatase nanocrystals. a) By analogy to alkoxide ligands on molecular TiO<sub>2</sub> clusters, **2'** is shown bound via μ<sub>2</sub>-O or μ<sub>3</sub>-O linkages to a facet perpendicular to (101) planes of anatase (O: red, Ti: yellow, W: green). b) Forward and reverse differential pulse voltammograms (versus Ag/AgCl, 3 M NaCl) of **2'**-capping ligands on anatase nanocrystals in 0.2 M aqueous LiClO<sub>4</sub>.

Moreover, the redox properties of the POM capping ligands can be rationally tuned. This was demonstrated by reacting amorphous TiO<sub>2</sub>(s) with α-SiW<sub>11</sub>O<sub>39</sub><sup>8−</sup> (K<sup>+</sup> salt), thus increasing the negative charges of the resulting capping ligands by one unit (characterization data are given in the Supporting Information, Figure S14). Consistent with established correlations between anion charge and reduction potential,<sup>[29]</sup> the first cathodic wave was shifted by ca. 175 mV in the negative direction (Supporting Information, Figure S14 f).<sup>[30]</sup>

Finally, the reduction potential of the POM ligand has a profound effect on photocatalytic activity. For example, under UV irradiation (150 W Xe lamp) in 10 vol % MeOH in water, H<sub>2</sub> evolution proceeds at 725 μmol g<sup>−1</sup> h<sup>−1</sup> for [α-SiW<sub>11</sub>O<sub>39</sub>Ti]−O<sup>−</sup>-capped NCs (per g of TiO<sub>2</sub>), and increases to 1500 μmol g<sup>−1</sup> h<sup>−1</sup> for the **2'**-capped NCs (Figure 7; see the Supporting Information for details). These rates are an order of magnitude larger than the values of 78 and 138 μmol g<sup>−1</sup> h<sup>−1</sup> obtained under identical conditions for commercial anatase and pure **2**, respectively, revealing dramatically enhanced reactivity upon covalent attachment of the POMs to the TiO<sub>2</sub>-NC cores.

Interestingly, the **2'**-capped NCs are much more effective than the [α-SiW<sub>11</sub>O<sub>39</sub>Ti]−O<sup>−</sup>-capped NCs. The **2'** ligands possess more positive reduction potentials than the [α-

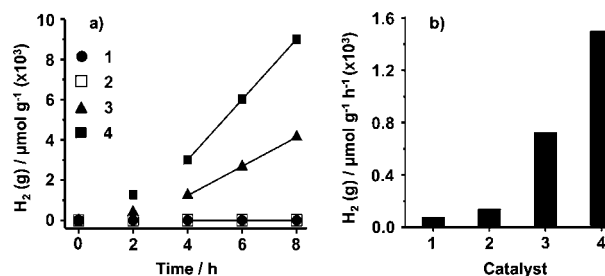


**Figure 7.** a) Photocatalytic H<sub>2</sub> evolution in as a function of time per gram quantity of: 1) commercial anatase, 2) pure [α-PW<sub>11</sub>O<sub>39</sub>]<sup>5−</sup> (Na<sup>+</sup> salt), 3) TiO<sub>2</sub> in [α-SiW<sub>11</sub>O<sub>39</sub>Ti]−O<sup>−</sup>-capped anatase NCs, and 4) TiO<sub>2</sub> in **2'**-capped anatase NCs. b) Rates of H<sub>2</sub> production, that is, slopes of the lines indicated in panel (a) (all with R<sup>2</sup> values of 0.999), after an induction period observed for both types of POM-capped NCs.

SiW<sub>11</sub>O<sub>39</sub>Ti]–O<sup>–</sup> ligands, and hence, are more effective electron acceptors. In principle, this could facilitate charge separation under photocatalytic conditions by more efficiently “trapping” photoexcited electrons. While future studies will address this in detail, the POM ligands could play an electron-accepting role analogous to that of platinum(0) nanoparticles routinely deposited on TiO<sub>2</sub> for numerous applications.<sup>[31]</sup> Unlike platinum(0), however, the electron-accepting properties of the POM ligands can be rationally tuned.

In summary, direct coordination of numerous polyoxometalate cluster anions to the surfaces of anatase-TiO<sub>2</sub> nanocrystals gives stable macroanion-like assemblies, which can be isolated as their alkali-metal cation or *n*-R<sub>4</sub>N<sup>+</sup> salts, and subsequently re-dissolved in water or organic solvents. And, just as traditional ligands control catalytically active metal centers in molecular complexes, the tunable redox chemistry of covalently attached POM capping ligands provides new options for rationally modifying the reactions of metal oxide semiconductor cores. More generally, the covalent attachment of redox-active POM capping ligands to nanocrystals of titanium and other transition-metal oxides promises access to a new family of catalytically active assemblies uniquely situated at the interface between molecular macroanions and traditional colloidal nanoparticles.

**Keywords:** electron transfer · hybrid materials · nanostructures · polyoxometalates · titanium dioxide

- [1] For references to a wide variety of structures and applications, see: *special issue on Polyoxometalate Cluster Science*, (Eds.: L. Cronin, A. Müller), *Chem. Soc. Rev.* **2012**, *41*, 7325–7648.
- [2] a) K. Nomiya, Y. Sakai, S. Matsunaga, *Eur. J. Inorg. Chem.* **2011**, 179–196; b) T. McGlone, L. Vila-Nadal, H. N. Miras, D.-L. Long, J. M. Poblet, L. Cronin, *Dalton Trans.* **2010**, *39*, 11599–11604; c) E. M. Villa, C. A. Ohlin, W. H. Casey, *J. Am. Chem. Soc.* **2010**, *132*, 5264–5272; d) G. A. Al-Kadamany, F. Hussain, S. S. Mal, M. H. Dickman, N. Leclerc-Laronze, J. Marrot, E. Cadot, U. Kortz, *Inorg. Chem.* **2008**, *47*, 8574–8576; e) R. J. Errington, S. S. Petkar, P. S. Middleton, W. McFarlane, W. Clegg, R. A. Coxall, R. W. Harrington, *Dalton Trans.* **2007**, 5211–5222; f) L. G. Detsuheva, M. A. Fedotov, L. I. Kuznetsova, A. A. Vlasov, V. A. Likhonov, *Russ. Chem. Bull.* **1997**, *46*, 874–880; g) T. Yamase, T. Ozeki, H. Sakamoto, S. Nishiyama, A. Yamamoto, *Bull. Chem. Soc. Jpn.* **1993**, *66*, 103–108; h) P. J. Dommelle, W. H. Knoch, *Inorg. Chem.* **1983**, *22*, 818–822; i) C. Tourne, C. R. Acad. Sci., Paris, Ser. C **1968**, *266*, 702–704.
- [3] T. Yamase, M. Sugeta, *Inorg. Chim. Acta* **1990**, *172*, 131–134.
- [4] a) O. A. Kholdeeva, *Eur. J. Inorg. Chem.* **2013**, *2013*, 1595–1605; b) N. S. Antonova, J. J. Carbo, U. Kortz, O. A. Kholdeeva, J. M. Poblet, *J. Am. Chem. Soc.* **2010**, *132*, 7488–7497; c) Y. Goto, K. Kamata, K. Yamaguchi, K. Uehara, S. Hikichi, N. Mizuno, *Inorg. Chem.* **2006**, *45*, 2347–2356; d) C. N. Kato, S. Negishi, K. Yoshida, K. Hayashi, K. Nomiya, *Appl. Catal. A* **2005**, *292*, 97–104; e) O. A. Kholdeeva, G. M. Maksimov, R. I. Maksimovskaya, L. A. Kovaleva, M. A. Fedotov, V. A. Grigoriev, C. L. Hill, *Inorg. Chem.* **2000**, *39*, 3828–3837; f) T. Yamase, E. Ishikawa, Y. Asai, S. Kanai, *J. Mol. Catal. A* **1996**, *114*, 237–245.
- [5] Y. Sakai, K. Yoza, C. N. Kato, K. Nomiya, *Chem. Eur. J.* **2003**, *9*, 4077–4083.
- [6] a) P. Coppens, Y. Chen, E. Trzop, *Chem. Rev.* **2014**, *114*, 9645–9661; b) L. Rozes, C. Sanchez, *Chem. Soc. Rev.* **2011**, *40*, 1006–1030.
- [7] R. C. Snoeberger, K. J. Young, J. Tang, L. J. Allen, R. H. Crabtree, G. W. Brudvig, P. Coppens, V. S. Batista, J. B. Benedict, *J. Am. Chem. Soc.* **2012**, *134*, 8911–8917.
- [8] These too are undergoing rapid development. For impressive examples, see: J. Huang, W. Liu, D. S. Dolzhnikov, L. Protesescu, M. V. Kovalenko, B. Koo, S. Chattopadhyay, E. V. Shchenchenko, D. V. Talapin, *ACS Nano* **2014**, *8*, 9388–9402.
- [9] For recent advances in electron-transfer reactions of TiO<sub>2</sub> and Fe<sub>3</sub>O<sub>4</sub> nanoparticles, respectively, see: a) J. N. Schrauben, R. Hayoun, C. N. Valdez, M. Braten, L. Fridley, J. M. Mayer, *Science* **2012**, *336*, 1298–1301; b) J. J. P. Roberts, J. A. Westgard, L. M. Cooper, R. W. Murray, *J. Am. Chem. Soc.* **2014**, *136*, 10783–10789.
- [10] As shown in Scheme 1, the four H<sup>+</sup> ions liberated by the hydrolysis of TTIP are consumed by the isopropoxide ligands, giving four equivalents of isopropanol with no change in the pH of the solution.
- [11] a) Y. Matsuki, Y. Mouri, Y. Sakai, S. Matsunaga, K. Nomiya, *Eur. J. Inorg. Chem.* **2013**, 1754–1761; b) G. Maksimov, R. Maksimovskaya, O. Kholdeeva, M. Fedotov, V. Zaikovskii, V. Vasil'ev, S. Arzumanov, *J. Struct. Chem.* **2009**, *50*, 618–627.
- [12] U. Vukičević, S. Ziemian, A. Bismarck, M. S. P. Shaffer, *J. Mater. Chem.* **2008**, *18*, 3448–3453.
- [13] a) Y. Rao, B. Antalek, J. Minter, T. Mourey, T. Blanton, G. Slater, L. Slater, J. Fornalik, *Langmuir* **2009**, *25*, 12713–12720; b) Joint Committee on Powder Diffraction Standards, Powder Diffraction File, Card No. 21–1272; c) Y. Liao, W. Que, Q. Jia, Y. He, J. Zhang, P. Zhong, *J. Mater. Chem.* **2012**, *22*, 7937–7944.
- [14] D. B. Williams, C. B. Carter, *Transmission Electron Microscopy: A Textbook for Materials Science*, 2nd ed., Springer, New York, **2009**.
- [15] H. P. Klug, L. E. Alexander, *X-Ray diffraction Procedures*, 2nd ed., Wiley, New York, **1974**.
- [16] Although not clearly discerned in TEM or HRTEM images of dry samples, cryo-TEM imaging effectively reveals the more-electron-dense 1 nm polytungstate ligands.
- [17] C. Rocchiccioli-Deltcheff, R. Thouvenot, *J. Chem. Res. Syn.* **1977**, 46–47.
- [18] Relative to the bulk material (that is, which would include the mass of TiO<sub>2</sub>), the reported uncertainty is equivalent to ±0.1 mass % P.
- [19] G. Schwarzenbach, J. Muehlebach, K. Mueller, *Inorg. Chem.* **1970**, *9*, 2381–2390.
- [20] The <sup>31</sup>P NMR spectrum (after overnight acquisition) contains a sharp signal at –13.96 ppm, precisely as expected for [PTiW<sub>11</sub>O<sub>40</sub>]<sup>5–</sup> (**2**) upon acid condensation in strongly acidic solution (Supporting Information, Figure S8).
- [21] a) O. Zeiri, Y. Wang, A. Neyman, F. Stellacci, I. A. Weinstock, *Angew. Chem. Int. Ed.* **2013**, *52*, 968–972; *Angew. Chem.* **2013**, *125*, 1002–1006; b) Y. Wang, O. Zeiri, A. Neyman, F. Stellacci, I. A. Weinstock, *ACS Nano* **2012**, *6*, 629–640; c) Y. Wang, A. Neyman, E. Arkhangelsky, V. Gitis, L. Meshi, I. A. Weinstock, *J. Am. Chem. Soc.* **2009**, *131*, 17412–17422.
- [22] The calculation was carried out as shown in Ref. [21c].
- [23] a) Y. Wang, I. A. Weinstock, *Chem. Soc. Rev.* **2012**, *41*, 7479–7496; b) Y. Wang, O. Zeiri, S. Sharet, I. A. Weinstock, *Inorg. Chem.* **2012**, *51*, 7436–7438.
- [24] X.-Q. Chen, W.-H. Shen, *Chem. Eng. Technol.* **2008**, *31*, 1277–1281.
- [25] After 3 h at room temperature, the NCs were removed by precipitation (by NaCl addition and centrifugation), and the supernatant solution was concentrated from 10 to 3 mL and treated with H<sub>2</sub>O<sub>2</sub>. If the **2'** cluster anions were electrostatically associated with the NCs, anion exchange with the relatively large

concentration of  $[\alpha\text{-AlW}_{12}\text{O}_{40}]^{5-}$  would have caused extensive release of **2'** to the bulk solution. However, no titanium–peroxo complexes **3** were detected by UV/Vis spectroscopy (Supporting Information, Figure S11). Notably, exchange of only about 5 % of the POM ligands **2'** would have given rise to a detectable absorbance band at 400 nm.

- [26] The situation is similar to that of alkanethiolate-protected Au nanoparticles (RS-AuNPs): Many years, and thousands of published articles, after discovery of the RS-AuNPs themselves, the “staple” motif of RS binding was determined from molecular  $\text{Au}_{25}(\text{SR})_{18}$  and  $\text{Au}_{102}(\text{SR})_{44}$  clusters; see, respectively: a) M. W. Heaven, A. Dass, P. S. White, K. M. Holt, R. W. Murray, *J. Am. Chem. Soc.* **2008**, *130*, 3754–3755; b) P. D. Jadzinsky, G. Calero, C. J. Ackerson, D. A. Bushnell, R. D. Kornberg, *Science* **2007**, *318*, 430–433.
- [27] Functionalized organic ligands are now being investigated as electron-donating sensitizers for molecular  $\text{TiO}_2$  clusters; see Ref. [7].
- [28] The implied current amplification may be an ensemble effect, as in: C. A. Beasley, R. W. Murray, *Langmuir* **2009**, *25*, 10370–10375.
- [29] a) O. Snir, Y. Wang, M. E. Tuckerman, Y. V. Geletii, I. A. Weinstock, *J. Am. Chem. Soc.* **2010**, *132*, 11678–11691; b) J. J. Altenau, M. T. Pope, R. A. Prados, H. So, *Inorg. Chem.* **1975**, *14*, 417–421.
- [30] For comparison, the first one-electron reduction potential of  $\alpha\text{-SiW}_{12}\text{O}_{40}^{4-}$  is about 190 mV more negative than that of  $\alpha\text{-PW}_{12}\text{O}_{40}^{3-}$ .
- [31] J. Schneider, M. Matsuoka, M. Takeuchi, J. Zhang, Y. Horiuchi, M. Anpo, D. W. Bahnemann, *Chem. Rev.* **2014**, *114*, 9919–9986.

Received: March 1, 2015

Published online: ■ ■ ■ ■ ■, ■ ■ ■ ■ ■



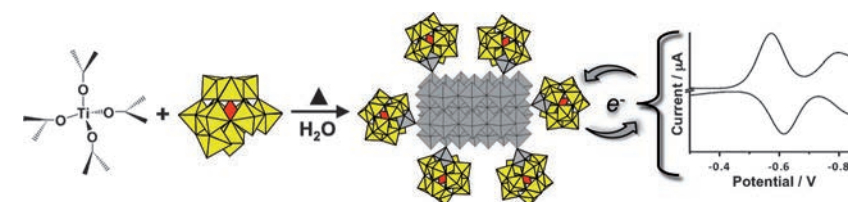
# Communications



## Hybrid Materials

M. Raula, G. Gan Or, M. Saganovich,  
O. Zeiri, Y. Wang, M. R. Chierotti,  
R. Gobetto,  
I. A. Weinstock\* ———— ■■■■—■■■■

Polyoxometalate Complexes of Anatase-Titanium Dioxide Cores in Water



**Redox-active ligands for TiO<sub>2</sub>:** Polyoxometalate (POM) electron acceptors serve as covalently coordinated inorganic ligands for anatase-TiO<sub>2</sub> nanocrystals, giving assemblies positioned between molecular macroanions and traditional

colloidal nanoparticles. The POM ligands have tunable redox potentials, providing options for controlling reactions of soluble metal oxide semiconductor nanocrystals.

## Supporting Information

German Edition: DOI:

### **Polyoxometalate Complexes of Anatase-Titanium Dioxide Cores in Water\*\***

*Manoj Raula, Gal Gan Or, Marina Saganovich, Offer Zeiri, Yifeng Wang, Michele R. Chierotti, Roberto Gobetto, and Ira A. Weinstock\**

anie\_201501941\_sm\_miscellaneous\_information.pdf



## Contents

### Materials and methods

- Figure S1.** P-31 NMR spectra obtained after reaction of amorphous  $\text{TiO}_2(\text{s})$  with  $\text{Na}_7[\alpha\text{-PW}_{11}\text{O}_{39}]$  ( $\text{Na}_7\mathbf{1}$ ).
- Figure S2.** Dynamic light scattering (DLS) data before and after dialysis and after four cycles of precipitation and re-dissolution in water.
- Figure S3.** Characterization of the anatase- $\text{TiO}_2$  nanocrystal (NC) cores.
- Figure S4.** Cryo-TEM images of POM-bound anatase- $\text{TiO}_2$  NCs, and of an anatase- $\text{TiO}_2$  NC with no POMs present.
- Figure S5.** HAADF-STEM images and EDX “spot analysis” of POM-bound anatase- $\text{TiO}_2$  NCs.
- Figure S6.** Unprocessed and baseline-corrected FTIR spectra of POM-bound anatase- $\text{TiO}_2$  NCs.
- Figure S7.** Solid-state  $^{31}\text{P}$  MAS NMR spectroscopic study of POM-bound anatase- $\text{TiO}_2$  NCs.
- Figure S8.** ESI mass spectrum of  $[\text{PTiW}_{11}\text{O}_{40}]^{5-}$  observed after digesting the  $\text{TiO}_2$  cores with HCl.
- Figure S9.** Determination of atom-percentages of W and Ti by EDX spectroscopy.
- Table S1.** Calculated atom-percentages of W and Ti.
- Figure S10.** Observation of POM-bound anatase- $\text{TiO}_2$  NCs in MeOH after cation exchange with  $n\text{-Bu}_4\text{N}^+$ .
- Figure S11.** UV-vis spectra showing that bound POM ligands *do not* exchange with added  $[\alpha\text{-AlW}_{12}\text{O}_{40}]^{5-}$ .
- Figure S12.** UV-vis absorbance spectra of POM-containing supernatant solution after mild HCl etching of POM capping ligands ( $\mathbf{2'}$ ) from the anatase NCs.
- Figure S13.** Electrochemical data for  $[\alpha\text{-PW}_{11}\text{O}_{39}\text{Ti}]\text{-O}^-$ -bound anatase- $\text{TiO}_2$  NCs and related cluster anions.
- Figure S14.** Characterization and DPV of  $[\alpha\text{-SiW}_{11}\text{O}_{39}\text{Ti}]\text{-O}^-$ -bound anatase- $\text{TiO}_2$  NCs.
- Figure S15.** ESI mass spectral identification of  $[\alpha\text{-SiTiW}_{11}\text{O}_{40}]^{6-}$ , a by-product formed during the synthesis of  $[\alpha\text{-SiW}_{11}\text{O}_{39}\text{Ti}]\text{-O}^-$ -bound anatase- $\text{TiO}_2$  NCs.
- Discussion.** Comparison of the spectroscopic and electrochemical properties of the POM ligands in  $[\alpha\text{-PW}_{11}\text{O}_{39}\text{Ti}]\text{-O}^-$ -bound anatase- $\text{TiO}_2$  NCs with those of related heteropolytungstates.

## Materials and methods

**Materials.** Titanium(IV) tetra-isopropoxide (TTIP, 99.999%, Sigma-Aldrich, USA), isopropanol (Reagent Grade, Carlo Erba, France), NaCl (analytical grade, Frutarom, Israel), deuterium oxide (99.9% D, Cambridge Isotope Laboratories, UK), titanium(IV) dioxide (99% anatase, Alfa-Aesar), tetrabutylammonium bromide (TBABr, ACS reagent,  $\geq 98\%$ , Sigma-Aldrich, USA), acetonitrile (99.8%, Alfa-Aesar) HCl (analytical grade, Bio Lab, Ltd., Israel) and  $\text{H}_2\text{O}_2$  (30 v/v%, Bio Lab, Ltd., Israel) were used as received. Sodium tungstate dihydrate ( $\text{Na}_2\text{WO}_4 \cdot \text{H}_2\text{O}$ , extra pure) was purchased from Merck. Additional reagent-grade salts, acids and diethyl ether for polyoxometalate synthesis and reactions were obtained from commercial sources and used as received. Regenerated-cellulose dialysis membranes (45-mm flat-width tubes; 12–14000 Da MWCO) were purchased from VWR Scientific, treated before use to remove glycerin and traces of sulfur compounds, and stored in water at 5 °C. All water used for cleaning, synthesis and reactions was of high purity (18 M $\Omega$  resistivity) from a Millipore Direct-Q water-purification system.  $\text{Na}_7[\alpha\text{-PW}_{11}\text{O}_{39}] \cdot 12\text{H}_2\text{O}$ ,<sup>[1, 2]</sup>  $\text{Na}_5[\alpha\text{-PTiW}_{11}\text{O}_{40}] \cdot x\text{H}_2\text{O}$ ,<sup>[3]</sup>  $\text{K}_8[\alpha\text{-SiW}_{11}\text{O}_{39}] \cdot 13\text{H}_2\text{O}$ ,<sup>[4]</sup> and  $\text{H}_5[\alpha\text{-AlW}_{12}\text{O}_{40}] \cdot 12\text{H}_2\text{O}$ <sup>[5]</sup> were prepared by literature methods and checked by FTIR and  $^{31}\text{P}$ ,  $^{27}\text{Al}$  and  $^{29}\text{Si}$  NMR spectroscopy, the latter giving clean NMR spectra with signals at -10.8, -13.9, -84.9, and 72.1 ppm, respectively (ppm-reference solutions are given below).

**Instrumentation. General.** pH values were measured using a EuTech pH 510 Bench-Top pH meter. UV-vis spectra were acquired using a HP 8452A spectrophotometer equipped with a diode-array detector (190–1100 nm range). FTIR spectra were acquired from KBr pellets using a Nicolet Impact 410 spectrophotometer. Al-27 and  $^{31}\text{P}$  NMR spectra were acquired on a Bruker 400 MHz instrument, and  $^{29}\text{Si}$  NMR spectra were acquired on a Bruker 500 MHz instrument. Chemical-shift values were externally referenced, respectively, to 0.10 M  $\text{AlCl}_3$  ( $[\text{Al}(\text{H}_2\text{O})_6]^{3+}$ ), 1.0 M  $\text{H}_3\text{PO}_4$  and tetramethylsilane (TMS), all set to  $\delta = 0$  ppm, with internal lock signals tuned using  $\text{D}_2\text{O}$ . NMR spectral data were processed using Mnova version 5.1 (Mestrelab Research). Zeta potentials were measured using a ZEM 3600 Zetasizer (Malvern Instruments, Ltd). XRD data were obtained using a Panalytical Empyrean instrument using Cu K $\alpha$  radiation ( $\lambda = 1.5405$  Å), operated at 40 kV and 30 mA, and equipped with a position sensitive (PSD) X'Celerator detector. DLS data was collected at 25 °C on an ALV-CGS-8F instrument (ALV-GmbH, Germany) at 90 deg (unless otherwise indicated), and the CONTIN method was used to obtain hydrodynamic radii ( $R_h$ ). Prior to each measurement, solutions were filtered through 0.45 and/or 0.22  $\mu\text{m}$  polyvinylidene fluoride (PVDF) Millipore filters. Electrospray ionization mass spectra (ESI-MS) were recorded from a LTQ Orbitrap XL instrument (Thermo Scientific, with an accuracy of 0.1 amu) with a nanospray ion source. TBA-salt of the POMs were used to make a solution in pure acetonitrile and directly injected for the ESI-MS measurements. Evolved hydrogen (photocatalysis studies) was quantified using a Thermo Scientific Focus Gas Chromatograph (GC) to analyze headspace gases sampled via a gas-tight syringe from septa-sealed reaction vessels. The GC was equipped with a dedicated thermal-conductivity detector (TCD), Ar was used as the carrier gas, and peak areas were calibrated using Scotty gas calibration standards (1%  $\text{H}_2$  in  $\text{N}_2$ ; Restek Corp).

**Electron microscopy.** Samples for transmission electron microscopy (TEM) and high-resolution TEM (HRTEM) were prepared by pipetting 5–10  $\mu\text{L}$  of sample solutions onto carbon-coated Cu grids, and then allowing them to dry in air. In some cases, an SPS Spin150 spin coater was used to improve surface dispersion of solutes. TEM data were obtained using a FEI Tecnai 12 G2 electron microscope (120kV) equipped with a Gatan slow-scan camera. HRTEM data were obtained using a JEOL JEM-2100F instrument operated at an accelerating voltage of 200 kV.

**Cryogenic-TEM.** Samples for cryo-TEM imaging were prepared using a fully automated vitrification device (“Vitrobot”). First, 2.5–3  $\mu\text{L}$  of the sample solution was placed by pipette onto a glow-discharged 300 Mesh Cu grid covered with a lacey-carbon film (Ted Pella, 01883-F) held inside a 100% humidity chamber. The grid was then mechanically “blotted” and immediately plunged into liquid ethane (b.p. 185K) cooled by liquid nitrogen (b.p. 77K). Data were collected on the FEI Tecnai 12 G2 instrument (120kV) and the Gatan slow-scan camera, using a low-dose regime to slow down the crystallization of vitrified water and to delay

the formation of other artifacts due to beam damage. All images from both dry- and cryo-TEM (including electron diffraction patterns) were analyzed using Digital Micrograph Gatan Inc. software.

**Energy-dispersive X-ray spectroscopy (EDS) and scanning TEM microscopy (STEM-HAADF).** EDS analyses were performed using a JEOL JEM- 2100F TEM operating at 200 kV equipped with a JED-2300T energy dispersive X-ray spectrometer. Scanning TEM (STEM-HAADF) images were obtained using an annular dark-field JEOL detector (EM 24560). The probe size during the analysis was set to either 1 or 0.2 nm. Probe tracking (drift correction) contributed to the high spatial resolution, resulting in high sensitivity analysis at the nanometer scale. JEOL Analytical Station software (v. 3.8.0.21) was used for the EDS data analysis.

**Differential Pulse Voltammetry (DPV).** DPV was carried out using a CHI 760C potentiostat at  $25 \pm 2$  °C in 0.2 M LiClO<sub>4</sub> electrolyte solutions, fitted with 2-mm glassy-carbon, Pt-wire and Ag/AgCl (3 M NaCl)<sup>[6]</sup> working, counter and reference electrodes respectively. Prior to data acquisition, solutions were purged with purified N<sub>2</sub> for 30 min. The following parameters were used: scan rate = 100 mV/s, sample width = 20 ms, pulse amplitude = 60 mV, pulse period = (interval) 200 ms, quiet time = 2 s, and sensitivity = 10<sup>-6</sup> A/V. Routine cyclic voltammograms (CVs) were obtained under N<sub>2</sub> using the same cell and electrodes.

**Solid-State NMR spectroscopy.** Room temperature <sup>1</sup>H magic-angle spinning (MAS), <sup>31</sup>P Cross-Polarization MAS (CPMAS) and <sup>1</sup>H – <sup>31</sup>P heteronuclear-correlation (HETCOR) spectra were recorded on a Bruker AVANCE II 400 instrument operating at 400.23 and 162.02 MHz for <sup>1</sup>H and <sup>31</sup>P, respectively. For <sup>31</sup>P CPMAS and HETCOR experiments cylindrical 4-mm outer diameter (O.D.) zirconia rotors with a sample volume of 80 µL were employed and spun at 12 kHz. For <sup>31</sup>P CPMAS measurements, a ramp cross polarization pulse sequence was used with variable contact times (0.5 to 6.5 ms), a <sup>1</sup>H 90° pulse of 3.80 µs, an optimize recycle delay of 0.4 s, and 8600 transients. The two-pulse phase modulation (TPPM) decoupling scheme was used with a frequency field of 75 kHz. The 2D <sup>1</sup>H – <sup>31</sup>P HETCOR spectrum was measured according to the method of van Rossum et al.<sup>[7]</sup> The proton rf field strength used during the t1 delay for FSLG decoupling and during the acquisition for TPPM decoupling was 82 kHz (see ref. 7 for details). Two off-resonance pulses with opposite phases (i.e., +x, -x or +y, -y) during the FSLG decoupling were set to 9.25 µs. The contact time was 2 ms. The magic angle (54.78°) pulse length for protons was set at 2.0 µs. Quadrature detection was achieved by using the states-TPPI method. All the data for 40 t1 increments with 6656 scans were collected. The <sup>1</sup>H chemical shift scale in the HETCOR spectrum was corrected by a scaling factor of 3<sup>-1/2</sup>, because the <sup>1</sup>H chemical shift dispersion is scaled by a factor of 3<sup>-1/2</sup> during FSLG decoupling.

H-1 MAS experiments were performed on a 2.5-mm probe. The <sup>1</sup>H MAS spectra (<sup>1</sup>H 90° pulse = 2.5 µs; recycle delay = 0.3 s; 64 scans) were acquired at a spinning rate of 32 kHz with a DEPTH sequence ( $\pi/2$ - $\pi$ - $\pi$ ) used to suppress the probe-background signal.

Variable-temperature <sup>31</sup>P CPMAS (variable contact times = 1 and 8 ms; <sup>1</sup>H 90° pulse = 2.60 µs; recycle delay = 1 s; 2100 scans) and MAS (<sup>31</sup>P 90° pulse = 3.0 µs; recycle delay = 30 s; 240 scans) spectra were recorded on a Bruker Avance III 500 spectrometer and a wide bore 11.7 Tesla magnet with operational frequencies for <sup>1</sup>H and <sup>31</sup>P of 500.13 and 202.46 MHz, respectively. The sample was packed on a zirconia rotor of 4-mm O.D. and spun at a MAS rate of 10 kHz. <sup>1</sup>H and <sup>31</sup>P scales were calibrated indirectly to adamantane (<sup>1</sup>H signal at 1.87 ppm) and triphenylphosphine (<sup>31</sup>P signal at -9.4 ppm with respect to aqueous 85% H<sub>3</sub>PO<sub>4</sub>) as external standards.

#### **Synthesis of Na<sup>+</sup> salt of “[α-PW<sub>11</sub>O<sub>39</sub>Ti]–O<sup>-</sup>” (2'-) capped anatase-TiO<sub>2</sub> nanocrystals.**

**Preparation of [α-PW<sub>11</sub>O<sub>39</sub>Ti]–O<sup>-</sup> (2'-) capped anatase-TiO<sub>2</sub> nanocrystals (Na<sup>+</sup> salt).** Titanium(IV) tetra-isopropoxide (TTIP, 100 µL) was diluted with 900 µL of isopropanol, and 708 µL of this solution (68.2 mg, 0.24 mmol TTIP) was added dropwise with vigorous stirring to 367 mg (0.12 mmol) of Na<sub>7</sub>[α-PW<sub>11</sub>O<sub>39</sub>]·12H<sub>2</sub>O (**1**) in 29.3 mL water at ambient temperature. This gave 30 mL of a cloudy (milky white) pH-6.0 mixture, with a final concentrations of 8 mM Ti(IV) and 4 mM **1**. Heated for 20 h at 170 °C in a 45 mL Teflon-lined 316 stainless-steel reaction vessel gave an optically clear, colorless pH-6.5 solution with no precipitate.

**Isolation and purification of the 2'-capped anatase-TiO<sub>2</sub> nanocrystals.** The 30 mL solution was placed in a cellulose membrane and dialyzed against pure water (1 L) in a 2 L beaker for 60 h, during which

time, the water outside the dialysis membrane was replaced every 12-15 hours. This removed a significant amount of the polyoxometalate by-products, which consisted primarily of  $\alpha$ -PTiW<sub>11</sub>O<sub>40</sub><sup>5-</sup> (**2**) and isopolytungstates (see Figure S1 for <sup>31</sup>P NMR spectra and the balanced equation for the overall reaction). Any POMs remaining in the solution were removed by first precipitating the nano-sized POM-capped TiO<sub>2</sub> by addition of NaCl (to a final concentration of 2 M). Under these conditions, reversible aggregation of the 2'-capped anatase-TiO<sub>2</sub> nanocrystals (NCs) decreases their solubility in water, so that they can be separated from the supernatant solution by centrifugation (30 min at 6000 rpm). Notably, millimolar concentrations of the primary POM by-product, **2**, are fully soluble in 2 M NaCl. After decanting the supernatant solution by pipette, the product, a hydrated white solid (ca. 10 mg), was collected and dissolved in 10 mL of pure water, to give a clear, colorless solution. Two additional “washing” cycles of precipitation by addition of NaCl, followed by centrifugation and redissolution in pure water, were carried out to be certain that trace amounts of **2** were no longer present. (After dialysis and just one precipitation cycle, the amount of “free” **2** present in the supernatant solution was already below its detection limit by UV-spectroscopy, i.e., less than 2  $\mu$ M.) Alternatively, the dialysis step can be eliminated if a total of four “washing” cycles are carried out.

**Characterization of the reaction byproduct,  $\alpha$ -PTiW<sub>11</sub>O<sub>40</sub><sup>5-</sup> (**2**).** The <sup>31</sup>P NMR spectrum of the supernatant, containing the Ti(IV)-substituted byproduct, **2**, featured a signal at -13.9 ppm with a bandwidth of 7 Hz,<sup>[3],[8]</sup> identical to the reported values after adjusting for small differences in concentrations of phosphoric-acid reference solutions. Moreover, addition of pure (separately prepared) Na<sub>5</sub>[ $\alpha$ -PTiW<sub>11</sub>O<sub>40</sub>] enhanced the observed signal, with no change in its linewidth. After isolating a small amount of the byproduct by selective crystallization, its FTIR spectrum was identical to that of pure Na<sub>5</sub>[ $\alpha$ -PTiW<sub>11</sub>O<sub>40</sub>];<sup>[8]</sup> FTIR (KBr):  $\gamma_{as}(\text{P-O})$  1085 and 1066 cm<sup>-1</sup>,  $\gamma_{as}(\text{W=O})$  970 cm<sup>-1</sup>,  $\gamma_{as}(\text{W-O-W, inter-triad corner-sharing})$  885 cm<sup>-1</sup>, and  $\gamma_{as}(\text{W-O-W, intra-triad edge-sharing})$  800 cm<sup>-1</sup>. Addition of H<sub>2</sub>O<sub>2</sub> to the isolated byproduct resulted in a yellow solution with a UV-vis absorbance maximum and <sup>31</sup>P chemical shift corresponding to the peroxo derivative,<sup>[9]</sup> [ $\alpha$ -PTi(O<sub>2</sub>)W<sub>11</sub>O<sub>39</sub>]<sup>5-</sup>.

**Characterization of the 2'-capped anatase-TiO<sub>2</sub> nanocrystals.** Characterization of these unique assemblies, including the redox properties of the covalently attached POMs, is the topic of this article. Characterization of the TiO<sub>2</sub> cores was easily accomplished using routine solid-state methods. However, the characterization of ligands on the surfaces of colloidal particles in solution—let alone their atomic-level connectivity to the particle surface—is extraordinarily challenging. As described in the text, this was achieved using a variety of solid- and solution-state microscopic, diffraction, and spectroscopic methods, combined with chemical digestion / etching, cation- and (*attempted*) anion-exchange experiments, and electrochemistry.

**UV-vis spectroscopic analysis of POM capping ligands, and their reaction with H<sub>2</sub>O<sub>2</sub>, after cleavage from the TiO<sub>2</sub> surface by mild etching with HCl.** POM capping ligands, **2'**, were cleaved from the anatase-TiO<sub>2</sub> NCs by mild etching. For this, two solutions of the NCs (10 mL each; prepared and purified as described above) were treated at room temperature with conc. HCl to a final concentration of 4 M HCl, at which Ti(IV) atoms at the surface of the anatase NCs begin to dissolve. The procedure also results in aggregation of the etched TiO<sub>2</sub>, and after gently stirring the cloudy white solution for 2 h, a white precipitate was spun down by centrifugation. The supernatant was then removed by pipette and concentrated to dryness by rotary evaporation. After evaporation of the excess HCl(g), and redissolution of the residue in 5 mL of pure water, the pH was 1.5. The absorbance observed in the UV region by UV-vis spectroscopy was consistent with the presence of [ $\alpha$ -PTiW<sub>11</sub>O<sub>40</sub>]<sup>5-</sup> (see Figure S12). Notably, when twenty  $\mu$ L of 30% H<sub>2</sub>O<sub>2</sub> were then added, a slight yellow color appeared, and the UV-vis spectrum (absorbance at 400 nm) indicated conversion of **2** to the peroxo complex, [ $\alpha$ -PTi(O<sub>2</sub>)W<sub>11</sub>O<sub>39</sub>]<sup>5-</sup> (**3**) (Figure S12). Importantly, control experiments confirmed that the yellow color was not due to reaction of peroxide with small amounts of Ti(IV) liberated from the anatase NCs during etching by HCl.

**Isolation and ESI-MS identification of [ $\alpha$ -PTiW<sub>11</sub>O<sub>40</sub>]<sup>5-</sup> after HCl digestion of the TiO<sub>2</sub> cores of 2'-capped NCs.** To exhaustively cleave all the POM capping ligands, **2'**, from the anatase-TiO<sub>2</sub> NCs, the TiO<sub>2</sub> cores of the composite material were digested in conc. HCl. For this, a 20 mL volume of 2'-capped TiO<sub>2</sub> NCs (extensively purified as described above), were treated with conc. HCl at 90 °C for 2 h. During this

time, Ti(IV) atoms of the anatase NCs dissolved, giving a clear solution. A P-31 NMR spectrum was recorded from this solution (Figure S8). Next, 1 mL of a 100 mM aq solution of tetrabutylammonium bromide (TBABr) was added to the digested-NC solution. After a few minutes, the solution became slightly cloudy. A white solid was collected by centrifugation, washed several times with pure water, and dissolved in MeCN. If the MeCN solution was slightly cloudy, it was clarified by filtration through a 20 nm Millipore filter. The MeCN solution (or filtrate) then was used for ESI-MS analysis. A 1% v/v 10 mM  $\text{NH}_4\text{Cl}$  aq. solution was added to the MeCN solution to improve ionization.

**Surface-bound POM capping anions are not exchanged by  $\alpha\text{-AlW}_{12}\text{O}_{40}^{5-}$ .** One mL of 5 mM  $\text{H}_5[\alpha\text{-AlW}_{12}\text{O}_{40}]$  (aq) was added to 4 mL of purified 2'-capped anatase- $\text{TiO}_2$  NCs in water. The clear, colorless solution was stirred for 3 h, after which, NaCl was added to precipitate the POM-capped  $\text{TiO}_2$  NCs. Then, the white precipitate was spun down by centrifugation (30 min at 6000 rpm), and the supernatant was collected by pipette and treated with 20  $\mu\text{L}$  of 30 vol-%  $\text{H}_2\text{O}_2$ . No increase in absorbance was observed at ca. 400 nm, confirming that the Ti-substituted Keggin anions, **2**, were not exchanged from the anatase-NC surfaces by  $\alpha\text{-AlW}_{12}\text{O}_{40}^{5-}$  (see Figure S11).

**Transfer of 2'-capped anatase- $\text{TiO}_2$  NCs into organic solvent using  $n\text{-R}_4\text{N}^+$  counteranions.** After synthesis at 170  $^\circ\text{C}$ , the solution of 2'-capped anatase- $\text{TiO}_2$  NCs, was dialyzed against pure water. Once the by-product,  $\alpha\text{-PTiW}_{11}\text{O}_{40}^{5-}$  (**2**), was no longer observed by  $^{31}\text{P}$  NMR,  $n\text{-Bu}_4\text{N}^+\text{Br}^-$  (TBABr) was added to a final concentration of 5 mM, giving a white precipitate that was collected by centrifugation and washed three times with pure water. Upon addition of MeOH (10 mL), the white solid dissolved completely, giving an optically clear solution of organic-solvent soluble 2'-capped NCs. DLS and TEM data are provided in Figure S10. A similar method was used to prepare an  $n\text{-Octyl}_4\text{N}^+$  salt of the 2'-capped anatase- $\text{TiO}_2$  NCs, a white solid soluble in toluene,  $\text{CH}_2\text{Cl}_2$ , MeCN and THF.

**Differential Pulse Voltammetry (DPV).** Purified 2'-capped anatase- $\text{TiO}_2$  NCs were dissolved in 200 mM of aq  $\text{LiClO}_4$ , to a final  $\text{TiO}_2$ -NC concentration of 1.7  $\mu\text{M}$ .

**Preparation and isolation of “[ $\alpha\text{-SiW}_{11}\text{O}_{39}\text{Ti}$ ]-O $^-$ ” capped anatase- $\text{TiO}_2$  nanocrystals.** These were prepared using the same method as that described above for synthesis of 2'-capped anatase- $\text{TiO}_2$  NCs, except that  $\text{K}_8[\alpha\text{-SiW}_{11}\text{O}_{39}]$  was used in place of  $\text{Na}_7[\alpha\text{-PW}_{11}\text{O}_{39}]$  (**1**). After room-temperature addition of TTIP, the pH of the cloudy white solution was 6.5, and heating for 22 h at 170  $^\circ\text{C}$  gave a clear colorless solution with a final pH of 6.9. Purification and isolation were carried out as described above for the 2'-capped anatase- $\text{TiO}_2$  NCs. Characterization data are summarized in Figure S14.

**Photocatalytic production of  $\text{H}_2$ .** Photocatalytic  $\text{H}_2$  production was carried out in a three-mL gas-tight quartz cuvette connected to a upper glass bulb with a headspace volume of 16 mL. Carefully weighed samples of 2'- and [ $\alpha\text{-SiW}_{11}\text{O}_{39}\text{Ti}$ ]-O $^-$ -capped NCs, pure  $[\alpha\text{-PTiW}_{11}\text{O}_{40}]^{5-}$  and commercial anatase were each solubilized/dispersed in 10% v:v methanol/water solutions. Each solution was purged with pure  $\text{N}_2$  (g) for at least 30 min, and then irradiated for 8 h using a 150 W Xe lamp (USHIO inc. Japan).  $\text{H}_2$  in the headspace was quantified every two h by injecting 0.5 mL volumes into a gas chromatograph (Focus GC, Thermo Scientific) operating at isothermal conditions (40  $^\circ\text{C}$ ) using a ShinCarbon ST micropacked column (0.53 mm diameter, 2 m length) equipped with a thermal conductivity detector and Ar as carrier gas. Data reported in Figure 7 for the POM-capped NCs were calculated based on the  $\text{TiO}_2$  cores comprising 60% of the total mass of the assemblies (see Table S1 for details).



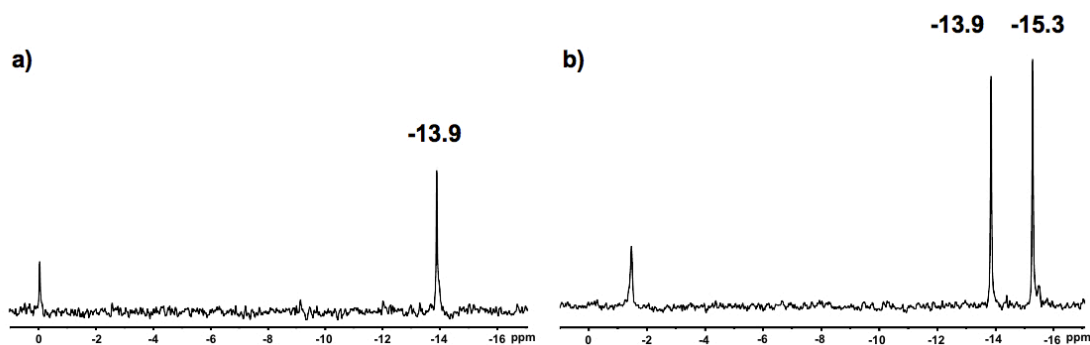
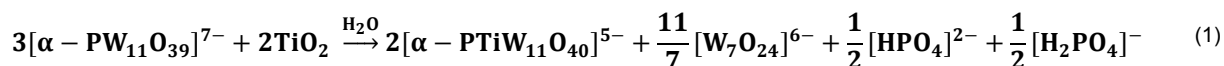


**Figure S1.** P-31 NMR spectra of reaction solutions. **a)** P-31 NMR spectrum obtained after reaction of amorphous  $\text{TiO}_2(\text{s})$  with  $\text{Na}_7[\alpha\text{-PW}_{11}\text{O}_{39}]$  (**Na<sub>7</sub>1**) for 20 h at 170 °C (see Experimental Methods). The reaction results in formation of  $[\alpha\text{-PTiW}_{11}\text{O}_{40}]^{5-}$  (**2**, -13.9 ppm), along with free phosphate (ca. 0 ppm), with a reproducible signal-intensity (integration) ratio of 2 equiv. of **2** per 1 equiv. of phosphate. All of the lacunary ion, **1** (a limited reagent) is consumed by reaction with the  $\text{TiO}_2(\text{s})$ . As this occurs, one equivalent of oxide ( $\text{O}^{2-}$ , or in water,  $2 \text{OH}^-$ ) is liberated for each equivalent of  $\text{TiO}_2(\text{s})$  that reacts to give **2**. (i.e., **2** contains a “ $\text{Ti}=\text{O}^{2+}$ ” moiety, and its formation liberates one equivalent of “ $\text{O}^{2-}$ ” from  $\text{TiO}_2$ ). As this occurs, the pH is maintained at 6.5 by hydrolysis of 1.33 mM (33%) of the 4 mM lacunary anion, **1**, present before heating. This results in the formation of phosphate (as seen in the  $^{31}\text{P}$  NMR spectrum), and must be accompanied by the co-formation of isopolytungstates. These were observed by adding HCl to decrease the pH to 0, followed by heating to induce condensation of the phosphate and isopolytungstates, to give the plenary Keggin ion  $[\alpha\text{-PW}_{12}\text{O}_{40}]^{3-}$ . Excess HCl was then removed by rotary evaporation (to dryness) and the solid was dissolved in  $\text{D}_2\text{O}$  (final pD = 1.9), and as expected, the  $^{31}\text{P}$  NMR spectrum (panel **b**) now revealed the presence of  $[\alpha\text{-PW}_{12}\text{O}_{40}]^{3-}$  ( $\delta = -15.3$  ppm), while the intensity of the phosphate signal decreased accordingly relative to that of **2** ( $\delta = -13.9$  ppm).

A balanced equation for the consumption of  $\text{TiO}_2$  by **1**, resulting in a 2:1 ratio of **2** to phosphates is given in eq. 1.



For simplicity, paratungstate-A,  $[\text{W}_7\text{O}_{24}]^{6-}$ , is shown; the actual solution may contain paratungstate-B, and/or isomeric mixtures of alpha and beta metatungstate. Starting from 8 mM amorphous  $\text{TiO}_2(\text{s})$  and 4 mM **1**, the final concentration of **2** formed is 2.66 mM, and the concentration of Ti(IV) in the anatase- $\text{TiO}_2$  nanocrystalline product in the finally obtained clear solution is 5.34 mM. Because ca. 100-200  $\mu\text{M}$  **2** remains bound to the anatase nanocrystals, the final concentration of “free” **2** present in the bulk solution is ca. 2.5 mM

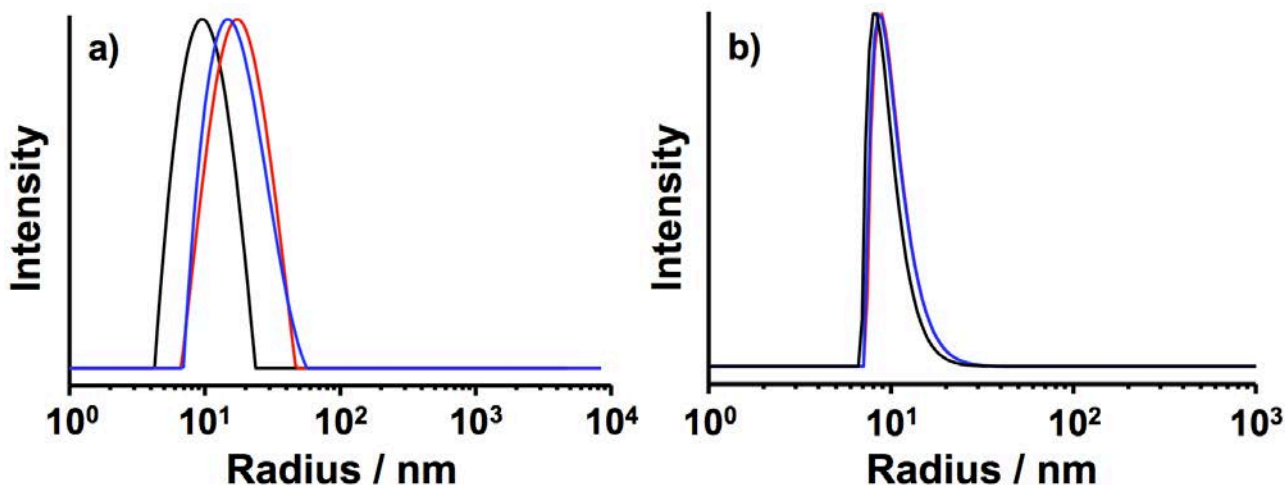


**Figure S2.** Dynamic light scattering (DLS) data after synthesis, after dialysis (14 days), and after four cycles of precipitation and re-dissolution in water. Panel **a)** shows the unweighted intensity profile of the three solutions (CONTIN method), while panel **b)** shows the number-weighted intensities. In both panels, the **black curve** indicates the DLS data obtained immediately after reaction of amorphous  $\text{TiO}_2(\text{s})$  with **Na<sub>7</sub>1** at 170 °C, the **blue curve** shows DLS results after treating the freshly prepared solution by dialysis against pure water for 14 days, and the **red curve** shows the DLS results obtained after two days of dialysis followed by four cycles of precipitation by 2 M NaCl and re-dissolution in water. In all cases, optically clear solutions were observed, with no precipitation or cloudiness. In the unweighted intensity plots (panel **a**), the average hydrodynamic radii increased only slightly, from ca. 9 (**black curve**) to 14 (**blue curve**) to 17 nm (**red curve**). Importantly, the number-weighted average radii remained effectively constant at  $9 \pm 1$  nm.

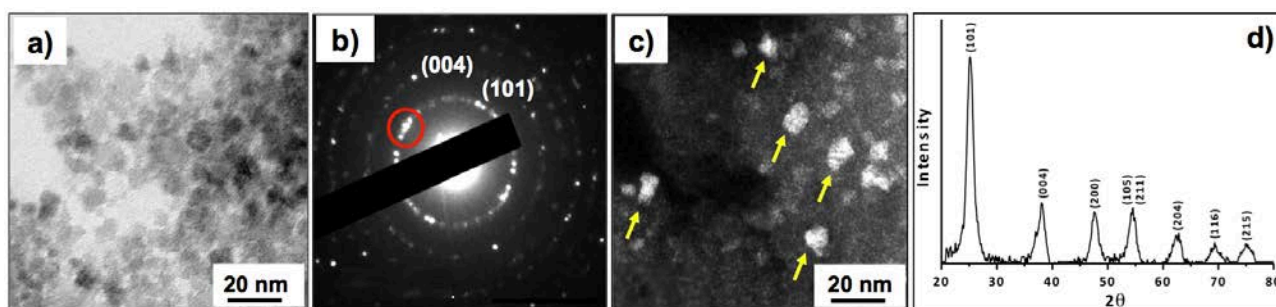


**Figure S3.** Characterization of the anatase-TiO<sub>2</sub> nanocrystal cores. a) Brightfield-TEM image of the purified nanoparticles; b) selected-area electron diffraction pattern of the particles in panel a); c) darkfield-TEM image obtained from the red-encircled part of the (101) ring in panel b). Here, diffraction from similarly oriented (101) reflection planes (red-encircled area in panel b), was used to selectively “illuminate” (and image) individual anatase nanocrystals (yellow arrows in panel c). d) Powder X-ray diffraction of the anatase NCs. The size of the anatase-TiO<sub>2</sub> crystallites ( $6.12 \pm 0.2$  nm) was determined using the Debye-Scherrer’s equation,  $L = 0.9\lambda/\beta\cos\theta$ , where,  $L$  is the size of the crystallites,  $\lambda$  is the X-ray wavelength (nm),  $\beta$  is the peak width at half maximum (in radians) of the most intense diffraction peak, and  $\theta$  is the Bragg angle of diffraction.

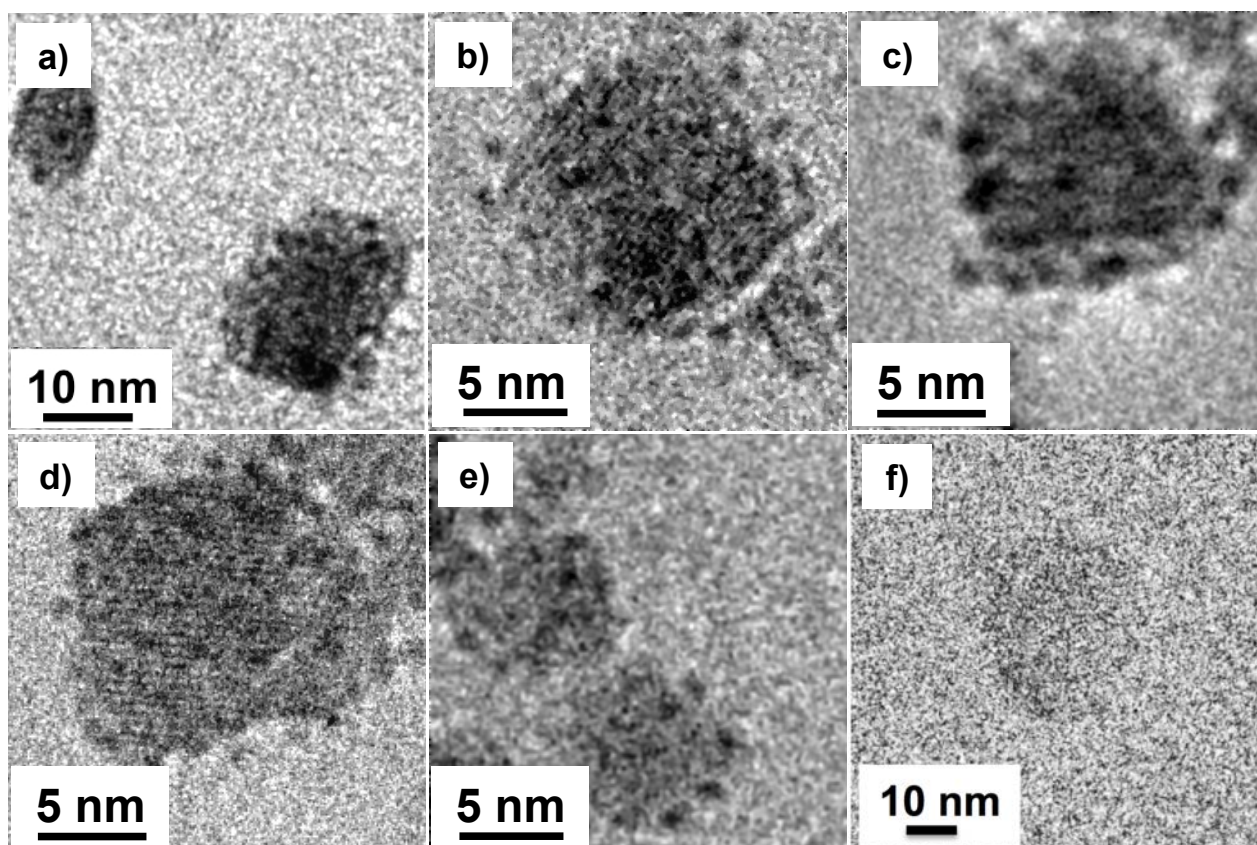


**Figure S4.** Cryo-TEM images. Panels a – e): Additional cryo-TEM images of 2'-capped anatase-TiO<sub>2</sub> nanocrystals. The dark and densely organized ca. 1-nm objects are heteropolytungstate cluster anions, closely related to  $[\alpha\text{-PTiW}_{11}\text{O}_{40}]^{5-}$  (2), and covalently attached to the anatase surface. f) For comparison, we provide here a cryo-TEM image of a much larger (ca. 30-40 nm sized) anatase-TiO<sub>2</sub> NC with no POMs present, prepared as described in ref. 10. Despite its larger size, the contrast due to TiO<sub>2</sub> alone (no W present) is much less than that of the heteropolytungstate-capped TiO<sub>2</sub> in the earlier panels. Notably, the cryo-TEM image in panel f is representative, and not due to less-than-optimal imaging parameters, e.g., to poor “under focus”. Rather, it results from the difference in electron density between Ti ( $Z = 22$ ) and W ( $Z = 74$ ).

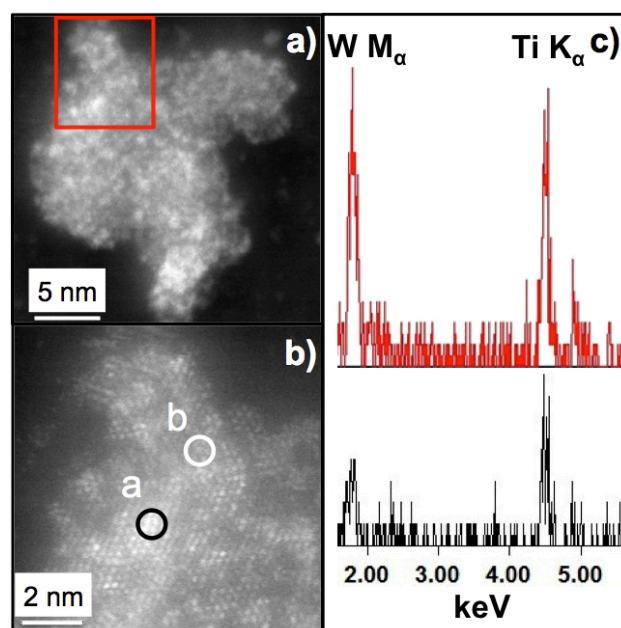


**Figure S5.** High angle annular dark field (HAADF) images and Energy dispersive X-ray (EDX) spectra of 2'-capped anatase-TiO<sub>2</sub> nanocrystals. **a)** HAADF image of several 2'-capped anatase-TiO<sub>2</sub> NCs, grouped together in the solid state. **b)** High magnification HAADF image obtained from the portion within the red box in panel **a)**. **c)** EDX spectra taken using a small 0.2 x 0.2 nm<sup>2</sup> spot size, from the black circle (labelled "a") and the white circle (labelled "b") in panel **b)**. The upper (red) spectrum in panel **c)** corresponds to the black circle, and is rich in tungsten. The lower (black) spectrum in panel **c)** corresponds to the white circle, and is poor in tungsten. This confirms that the brighter areas contain the heteropolytungstate cluster-anions, whereas the less-bright areas are predominantly TiO<sub>2</sub>.

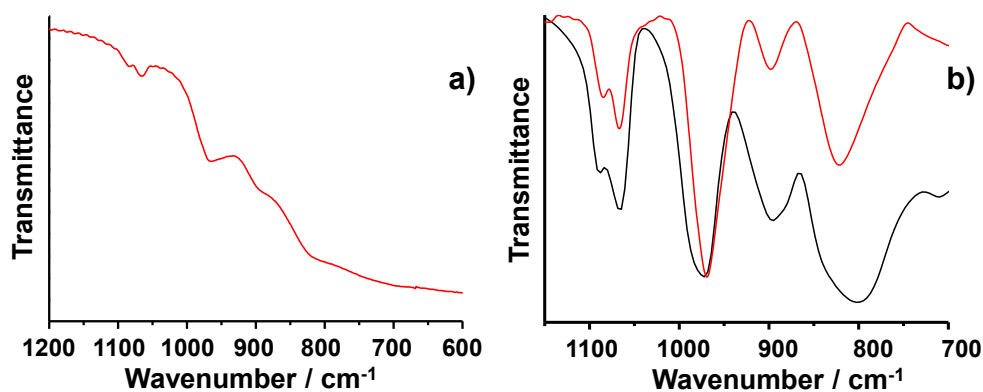


**Figure S6.** Unprocessed, **a)**, and baseline corrected (**b**, red curve) FTIR spectra of 2'-capped anatase-TiO<sub>2</sub> nanocrystals (KBr pellet). The black curve in panel **b)** is the FTIR spectrum of pure Na<sub>5</sub>[α-PTiW<sub>11</sub>O<sub>40</sub>]. Note (red curve in panel **b)** that upon baseline correction, the steep decrease in transmittance from ca. 950-800 cm<sup>-1</sup> (caused by TiO<sub>2</sub>), artificially decreases the relative intensity of the POM band at ca. 900 cm<sup>-1</sup>. This is helpful for understanding the baseline-corrected FTIR spectrum of the analogous material prepared using the mono-lacunary anion, [α-SiW<sub>11</sub>O<sub>39</sub>]<sup>6-</sup> (Figure S14, panel **d)**, in which the relative intensity of the corresponding band (at 907 cm<sup>-1</sup> in that case) appears even smaller than observed here for the 2'-capped anatase-TiO<sub>2</sub> nanocrystals.

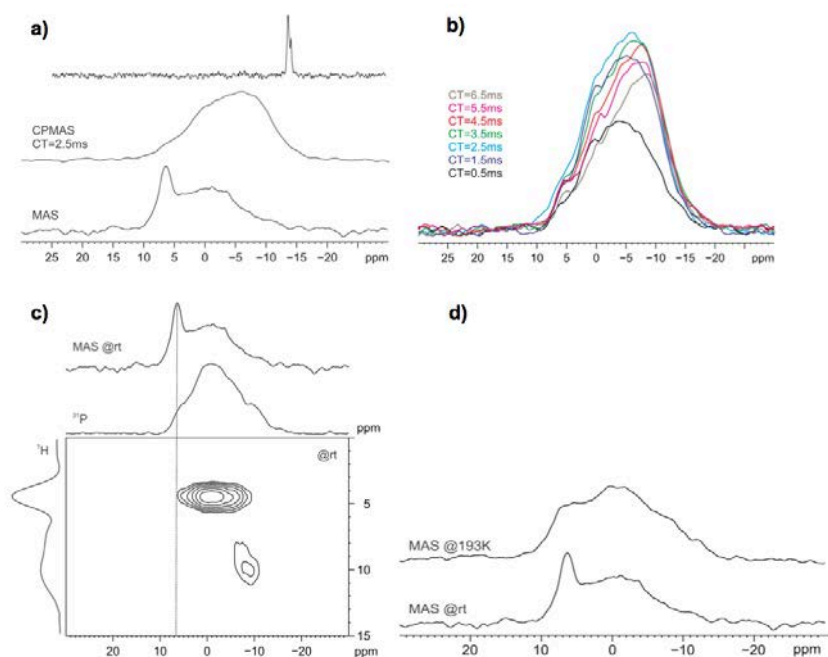


**Figure S7.** Solid-state magic-angle spinning (MAS)  $^{31}\text{P}$  NMR spectroscopic study of hydrated  $\text{Na}^+$  salts of POM-bound anatase- $\text{TiO}_2$  nanocrystals (POM- $\text{TiO}_2$ ). **a) Top:**  $^{31}\text{P}$  MAS NMR spectrum of pure  $\text{Na}_5\text{PTiW}_{11}\text{O}_{40}$ ; **middle:**  $^{31}\text{P}$  cross-polarization magic-angle spinning (CPMAS) NMR spectrum POM- $\text{TiO}_2$  (contact time = 2.5 ms); **bottom:**  $^{31}\text{P}$  MAS NMR spectrum of POM- $\text{TiO}_2$ . All three spectra were acquired at room temperature. **b)**  $^{31}\text{P}$  CPMAS NMR spectrum POM- $\text{TiO}_2$  acquired using a range of contact times (CTs). **c)** A two-dimensional  $^1\text{H}$ - $^{31}\text{P}$  frequency-switched Lee-Goldburg (FSLG)-decoupled heteronuclear-correlation (HETCOR) spectrum of POM- $\text{TiO}_2$  recorded at room temperature with a CT value of 2.0 ms (the  $^{31}\text{P}$  MAS NMR spectrum is shown on the same scale at the top). **d)**  $^{31}\text{P}$  MAS NMR spectra of POM- $\text{TiO}_2$  recorded at room temperature (**bottom**) and at 193K (**top**).

Based on published solid-state  $^{31}\text{P}$  NMR spectra of *intact*  $\alpha\text{-PW}_{12}\text{O}_{40}^{3-}$  salts on solid supports,<sup>[11, 12]</sup> a shift to higher frequencies is expected upon bonding of the POM ligands to the anatase- $\text{TiO}_2$  nanocrystals (NCs), and broadening of the shifted  $^{31}\text{P}$  NMR signals is expected to arise from heterogeneous local environments on the  $\text{TiO}_2$  surface (*cf.* Figure 3 in the text). The data provided here show that some of this broadening arises from differences in the specific local environments created by sodium counter cations and water molecules in the hydrated solid material. These effects are analogous to those observed by Misono in solid-state spectra of  $\text{H}_3[\alpha\text{-PW}_{12}\text{O}_{40}]$  not loaded on surfaces.<sup>[13]</sup>

The MAS  $^{31}\text{P}$  NMR spectrum of solid  $\text{Na}_5\text{PTiW}_{11}\text{O}_{40}$  (panel **a**, **top**) is more complex than the single  $^{31}\text{P}$  NMR signal observed in  $\text{D}_2\text{O}$  (see Figure 1d in the text). This situation is similar to that observed by Misono<sup>[13]</sup> for hydrated  $\text{H}_3[\alpha\text{-PW}_{12}\text{O}_{40}]$ . The  $\text{Ti(IV)}$ -substituted Keggin ion,  $\alpha\text{-PTiW}_{11}\text{O}_{40}^{5-}$ , was chosen as a starting point because it is structurally related to the  $[\alpha\text{-PW}_{11}\text{O}_{39}\text{Ti}]\text{-O}^-$  ligands, which we show (later in the text) are covalently bound to the anatase- $\text{TiO}_2$  NCs.

A comparison between  $^{31}\text{P}$  MAS and CPMAS spectra (panel **a**, **middle** and **bottom**) suggests the presence of different  $^{31}\text{P}$  sites associated with different molecules of bound  $[\alpha\text{-PW}_{11}\text{O}_{39}\text{Ti}]\text{-O}^-$  ligands. In particular, disappearance of the sharp peak at ca. 6.3 ppm on passing from MAS to CPMAS suggests that this P site is far from hydrogen atoms. Given the near-neutral pH values of the sample studied, this finding further rules out the presence of “phosphate” anions, as these would have to be fully deprotonated to account for the signal at 6.3 ppm (i.e., to be farther away from protons). Such a degree of deprotonation is not consistent with the near-neutral pH of the samples; note: phosphate is a much stronger base than the POM ligand. The distance dependence of the phenomena responsible for the differences between the MAS and CPMAS spectra are not well defined for heterogeneous materials. In molecular crystals, however, efficient polarization transfer is observed for distances closer than about 3-4 Angstroms. We understand the different proton distances observed in panel **a** to arise from different local concentrations and relative positions of hydrated  $\text{Na}^+$  counter-cations, and the affect of these on protonation of (relatively more basic) bridging-oxygen ligands of the bound POMs.

The dynamic cross-polarization (CP) (CPMAS experiment with different contact time (CT) (panel **b**), confirms the presence of different  $^{31}\text{P}$  sites. Indeed by varying the contact time the high-frequency region decreases in intensity while that of the low-frequency region increases. This behavior can be correlated to either different proton mobilities or different  $^1\text{H}$ - $^{31}\text{P}$  proximities in relation to the  $^{31}\text{P}$  environments. In a simple approximation of low proton mobility, by increasing the contact time,  $^{31}\text{P}$  signal intensities of regions close to hydrogen atoms increase until reaching a maximum, then the signal starts to decrease. Meanwhile  $^{31}\text{P}$  regions far from the protons are favored at shorter contact time.

The 2D  $^1\text{H}$ - $^{31}\text{P}$  heteronuclear correlation (HETCOR) experiment recorded at RT is shown in panel **c**, together with the  $^{31}\text{P}$  MAS spectrum for comparison. In the  $^1\text{H}$  part of the 2D spectrum two different types of proton environments are clearly distinguishable: one related to water molecules at ca. 4.45 ppm, and one related to either H-bonded protons (OH or water protons) or extremely acidic protons at ca. 10 ppm. The  $^1\text{H}$  resonance at 4.45 ppm (water environment)



correlates mainly with the  $^{31}\text{P}$  signal region centered at -1.0 ppm, whereas the  $^{31}\text{P}$  region centered at -8.7 ppm correlates with the  $^1\text{H}$  peak around 10 ppm.

RT and  $^{13}\text{C}$   $^{31}\text{P}$  spectra recorded at 202.45 MHz (500 spectrometer) are reported in panel **d**. They show the presence of mobility because in the low-temperature spectrum several environments are observable by the presence of shoulders (around 6.4, 4.2, 0.5, -1.0, -5.9, -8.7 and -11.8 ppm). The lower temperature (193K) represents the lowest temperature accessible with the available instrumentation. It is worth noting that in case of exchange or mobility, by increasing the magnetic field the static situation is expected at higher temperatures with respect to lower magnetic fields. By comparing our spectra with that reported by Misono and coworkers (Figure 5 in ref. [13]) we can suggest that in our case (at both temperatures) the chemical shift range is wider and shifted to higher frequencies. This results in a hiding of the four sharp peaks previously found. The broadening of the peaks can be due to the presence of many heterogeneous local sites on the  $\text{TiO}_2$  surface, while the shift to higher frequencies is caused by direct bonding to the anatase- $\text{TiO}_2$ .<sup>[11, 12]</sup> As discussed in the text, this bonding may involve bridging oxide linkages (i.e.,  $[\alpha\text{-PW}_{11}\text{O}_{39}\text{Ti}]-\mu_2\text{-O}^-$  or  $[\alpha\text{-PW}_{11}\text{O}_{39}\text{Ti}]-\mu_3\text{-O}^-$ ) to one and/or two Ti atoms at the  $\text{TiO}_2$  surface.

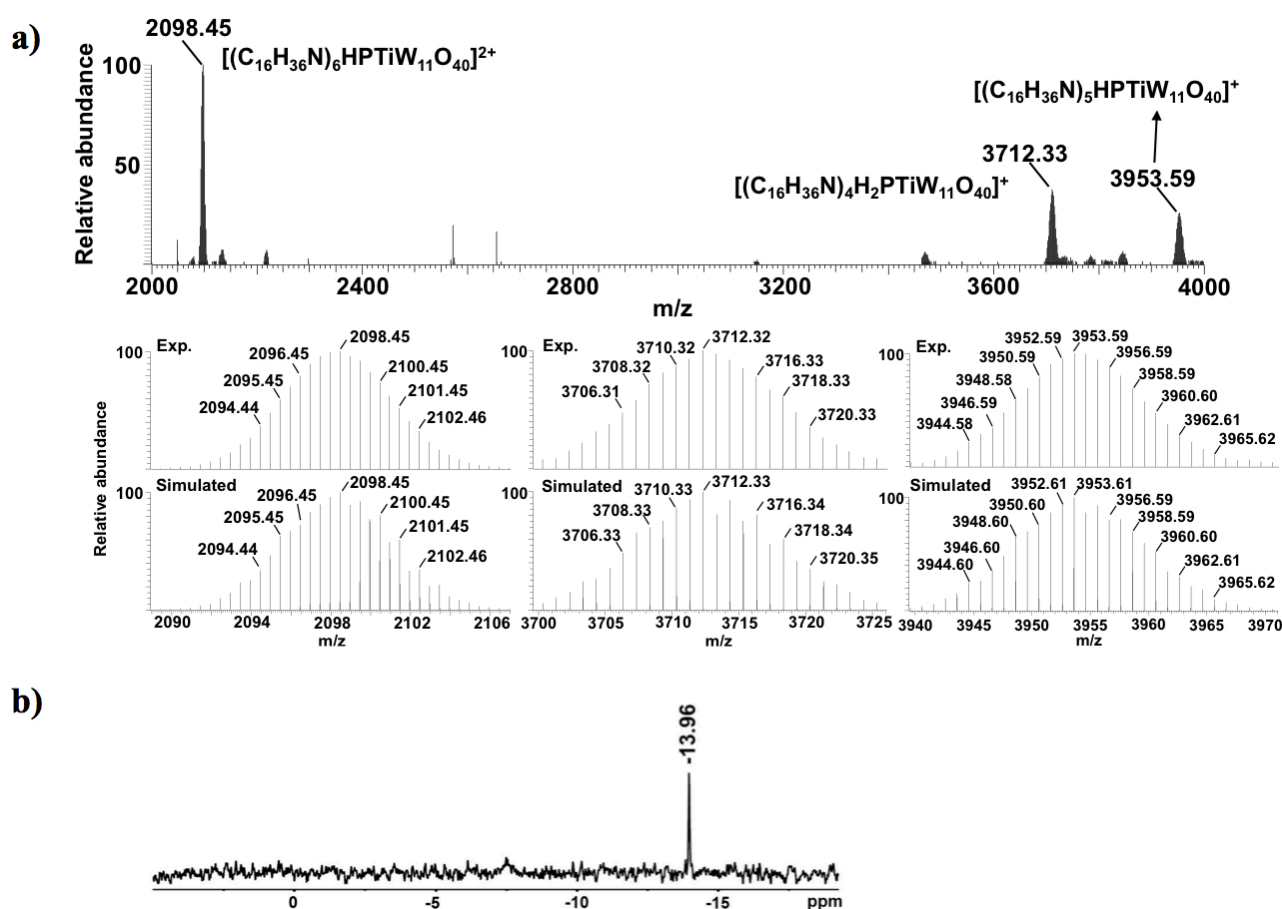


**Figure S8.** **a)** ESI mass spectrum obtained after digesting the 2'-capped anatase- $\text{TiO}_2$  nanocrystals using conc. HCl and then precipitating the  $n\text{-Bu}_4\text{N}$ -salt of the POMs, isolating it as a white solid, and dissolving the solid in acetonitrile (see experimental section above for details). The spectrum shows one 2+ ion (dominant set of peaks) and two 1+ "parent" ions. While the accuracy of the Orbitrap XL ESI-MS instrument is 0.1 amu, the tops of the envelopes actually match to within 0.02 amu in all three cases. Corresponding envelopes of experimental and simulated signals are provided below the full spectrum. As can be seen, the peaks from the experimental envelopes typically match to within 0.02 amu of those obtained in the simulations. In all cases, the observed ions are salts of the  $[\text{PTiW}_{11}\text{O}_{40}]^{5-}$  cluster (**2**). **b)** The  $^{31}\text{P}$  NMR spectrum of the solution obtained after digesting the 2'-capped anatase- $\text{TiO}_2$  nanocrystals by conc. HCl in  $\text{D}_2\text{O}$ . After concentrating to a small volume, the concentration of POM present was still very small (as expected). Hence, the  $^{31}\text{P}$  NMR spectral data were acquired for over 12 hours. At the large  $\text{H}^+$  concentration used (the pH was less than zero),  $[\text{PTiW}_{11}\text{O}_{40}]^{5-}$  is quantitatively condensed to  $[(\text{PTiW}_{11}\text{O}_{39})_2\text{O}]^{8-}$ . This is well documented by the Russian group from Novosibirsk (G. M. Maksimov, et. al. *J. Struct. Chem.*, **2009**, *50*, 618-627), and in impressive detail by the Japanese group headed by Nomiya; see: *Eur. J. Inorg. Chem.* **2013**, 1754–1761. According to Nomiya, the  $^{31}\text{P}$  NMR chemical shift of the dimeric (condensed) form of the cluster in mixed  $\text{H}_2\text{O}/\text{DMSO}$  and/or in  $\text{H}_2\text{O}$  is ca. 0.06 – 0.08 ppm upfield (more negative) than that of the monomeric ion. This difference in chemical shift has been independently confirmed in our hands in pure  $\text{D}_2\text{O}$  for both the monomeric and dimeric (condensed) structures. Accordingly, the chemical shift of the observed signal (-13.96 ppm relative to 85% phosphoric acid), obtained at a pH value less than zero, is 0.06 ppm more negative than the -13.9 ppm signal for the monomeric cluster,  $[\text{PTiW}_{11}\text{O}_{40}]^{5-}$ , whose spectrum appears in Figure 1d of the text.



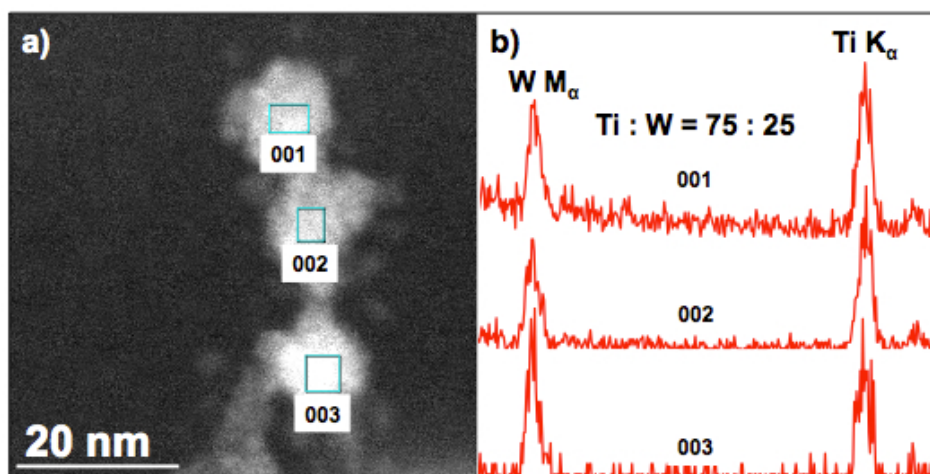


**Figure S9.** Representative HAADF images and EDX spectra used to determine atom-percentages of W and Ti. **a)** A HAADF image of particles in a dried sample of purified 2'-capped anatase-TiO<sub>2</sub> nanocrystals. **b)** EDX spectra obtained from areas "001", "002" and "003" in panel **a)** gave an average atom-percent of 75 ± 3 % Ti to 25 ± 3 % W.

**Table S1. Calculated Atom-Fractions<sup>a</sup> of Ti and W**

[Ti(IV)] (as TiO <sub>2</sub> )	0.00533 M
Density of TiO <sub>2</sub>	4.23 x 10 <sup>21</sup> g nm <sup>-3</sup>
Mol. Wt. of TiO <sub>2</sub>	79.87 g mol <sup>-1</sup>
Volume of TiO <sub>2</sub> solution	0.01500 L
Moles of Ti(IV)	8.00 x 10 <sup>-5</sup> mol
Mass of TiO <sub>2</sub> in solution	6.39 x 10 <sup>-3</sup> g
Volume of TiO <sub>2</sub>	1.51 x 10 <sup>18</sup> nm <sup>3</sup>
Volume of one TiO <sub>2</sub> NC	54.9 nm <sup>3</sup>
<b>No. of Ti atoms per NC</b>	<b>1,751</b>
No. of TiO <sub>2</sub> NCs	2.75E x 10 <sup>16</sup>
[TiO <sub>2</sub> ] NCs	3.04 x 10 <sup>-6</sup> M
Surface area of one TiO <sub>2</sub> NC	94.3 nm <sup>2</sup>
POM footprint on NC surface	1.78 nm <sup>2</sup>
[POM] (bound to NCs)	161.2 μM
<b>No. of POMs per NC</b>	<b>53</b>
Sum of W + Ti atoms / particle	2.33 x 10 <sup>3</sup>
<b>Atom/atom fraction of Ti</b>	<b>0.75</b>
<b>Atom/atom fraction of W</b>	<b>0.25</b>

<sup>a</sup> Values calculated are for an ideal rectangular-prismatic anatase-TiO<sub>2</sub> NC with dimensions (in nm) of 6.10 (L) x 4.00 (W) x 2.25 (H). As the height, H, of the NC varies from 1.7 to 3.1 nm, the atom-fractions of W and Ti vary by 6% (corresponding to the ±3% uncertainty based on different EDX measurements).

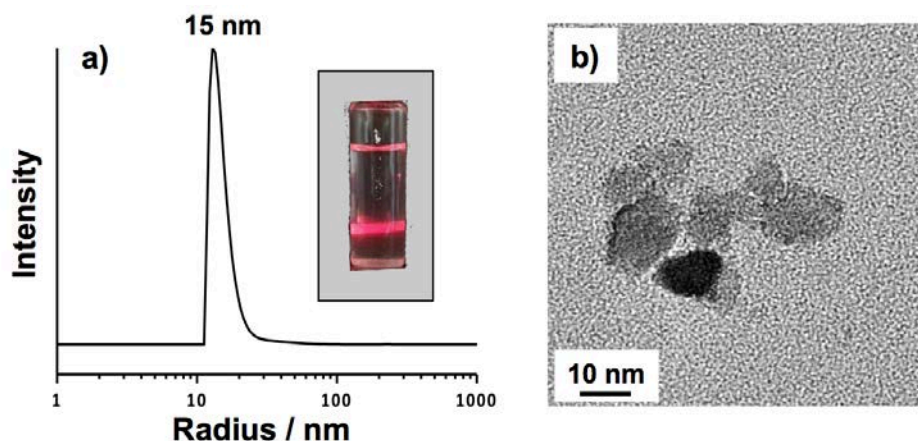


**Figure S10.** DLS data and TEM images of the  $n\text{-Bu}_4\text{N}^+$  salt of **2'**-capped anatase- $\text{TiO}_2$  nanocrystals in MeOH. **a)** DLS data (number weighted); **inset:** Rayleigh scattering from the clear methanolic solution, and **b)** a TEM micrograph of the dried methanolic solution.

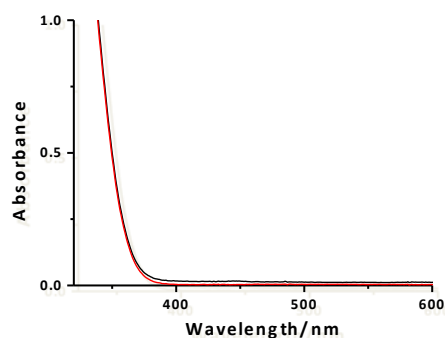


**Figure S11.** UV-vis absorbance spectra showing that bound POM ligands (**2'**) do not exchange with added  $[\text{AlW}_{12}\text{O}_{40}]^{5-}$ . **Black curve:** Spectrum of the **2'**-capped anatase- $\text{TiO}_2$  NCs in water with 1 mM  $\text{H}_5[\text{AlW}_{12}\text{O}_{40}]$ . **Red curve:** Spectrum obtained after using NaCl to precipitate the  $\text{TiO}_2$  NCs, and treating the supernatant solution with  $\text{H}_2\text{O}_2$ . No increase in absorbance was observed at ca. 400 nm, confirming that the Ti(IV)-substituted POM ligands (**2'**) were not exchanged by  $[\text{AlW}_{12}\text{O}_{40}]^{5-}$ . However, the attached POM ligands *can* be removed by room temperature etching with HCl, as shown immediately below (Figure S12).

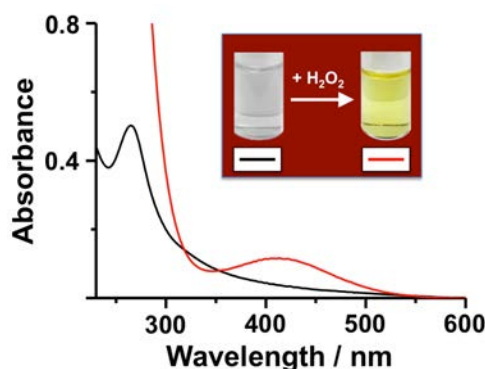


**Figure S12.** UV-vis absorbance spectra of POM-containing supernatant solution after mild HCl etching of POM capping ligands (**2'**) from the anatase NCs. During room temperature etching by HCl (final HCl concentration was 4 M), Ti ions at the surface of the anatase NCs begin to dissolve. The procedure also results in aggregation of the etched (and unprotected)  $\text{TiO}_2$ , and after gently stirring the cloudy white solution for 2 hours, a white precipitate was spun down by centrifugation. The supernatant was then removed by pipette and concentrated to dryness by rotary evaporation. After evaporation of the excess HCl (g), and redissolution of the residue in 5 mL of pure water, the final pH was 1.5. The UV-vis spectrum of this solution (black curve) was consistent with the presence of **2**, which upon addition of  $\text{H}_2\text{O}_2$  was converted to the peroxo complex,  $[\alpha\text{-PTi}(\text{O}_2)\text{W}_{11}\text{O}_{39}]^{5-}$  (**3**), indicated by a pale-yellow color and an absorbance maximum at ca. 400 nm (red curve and inset). Inset: Colorless and yellow solutions, before and after reaction with  $\text{H}_2\text{O}_2$  (concentrated for better visualization). Control experiments showed the new band was not due to reaction of  $\text{H}_2\text{O}_2$  with small amounts of Ti(IV) dissolved during etching by HCl.

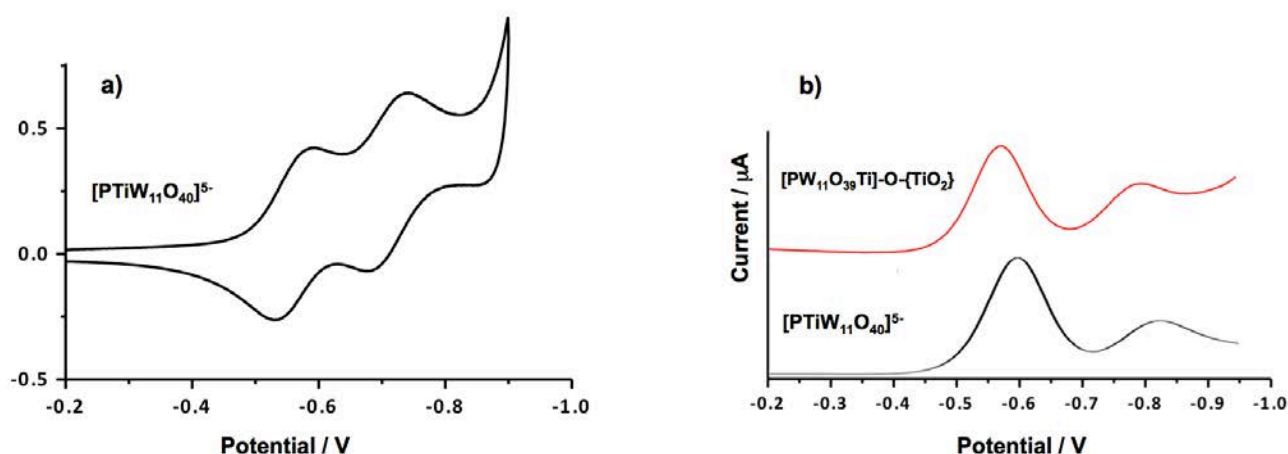


**Figure S13.** Cyclic and differential pulse voltammetry (CV & DPV) of  $[\alpha\text{-PW}_{11}\text{O}_{39}\text{Ti}]\text{-O}^-$ -bound anatase- $\text{TiO}_2$  NCs and related cluster anions. **a)** Cyclic voltammogram of  $[\alpha\text{-PTiW}_{11}\text{O}_{40}]^{5-}$  (**2**) in aq acetate buffer. **b)** Differential pulse voltammograms: of  $[\alpha\text{-PW}_{11}\text{O}_{39}\text{Ti}]\text{-O}^-$  (**2'**) capped anatase- $\text{TiO}_2$  NCs at pH 7 in 200 mM  $\text{LiClO}_4$  (**red curve**), and of free  $[\alpha\text{-PTiW}_{11}\text{O}_{40}]^{5-}$  (**2**; 100  $\mu\text{M}$ ) at pH 7 in 200 mM  $\text{LiClO}_4$  (**black curve**). The CV in panel **a** was obtained using both  $\text{LiClO}_4$  and acetate buffer, while the DPV data in panel **b** contained only  $\text{LiClO}_4$ . This affects the shape and relative intensities (total currents) of the first and second cathodic waves of the Ti-substituted POMs in panel **b**. (The addition of acetate buffer was avoided as it led to precipitation of the anatase assemblies.) Nevertheless, the potentials of both cathodic currents due to the bound POM in panel **b** (**2'**, **red curve**) are clearly different (more positive) than those of freely solvated  $[\alpha\text{-PTiW}_{11}\text{O}_{40}]^{5-}$  (**2**). While future studies will address the affect of different counter-cations and pH on the reduction potential(s) of the bound POM ligands, these data support assignment of the redox process shown in Figure 6 (text) to the bound  $[\alpha\text{-PW}_{11}\text{O}_{39}\text{Ti}]\text{-O}^-$  anions (**2'**), while simultaneously showing that the more negative cathodic wave (observed at ca. -800 mV) is due to the bound **2'** ligands, rather than to reduction of Ti(IV) in the anatase NCs.

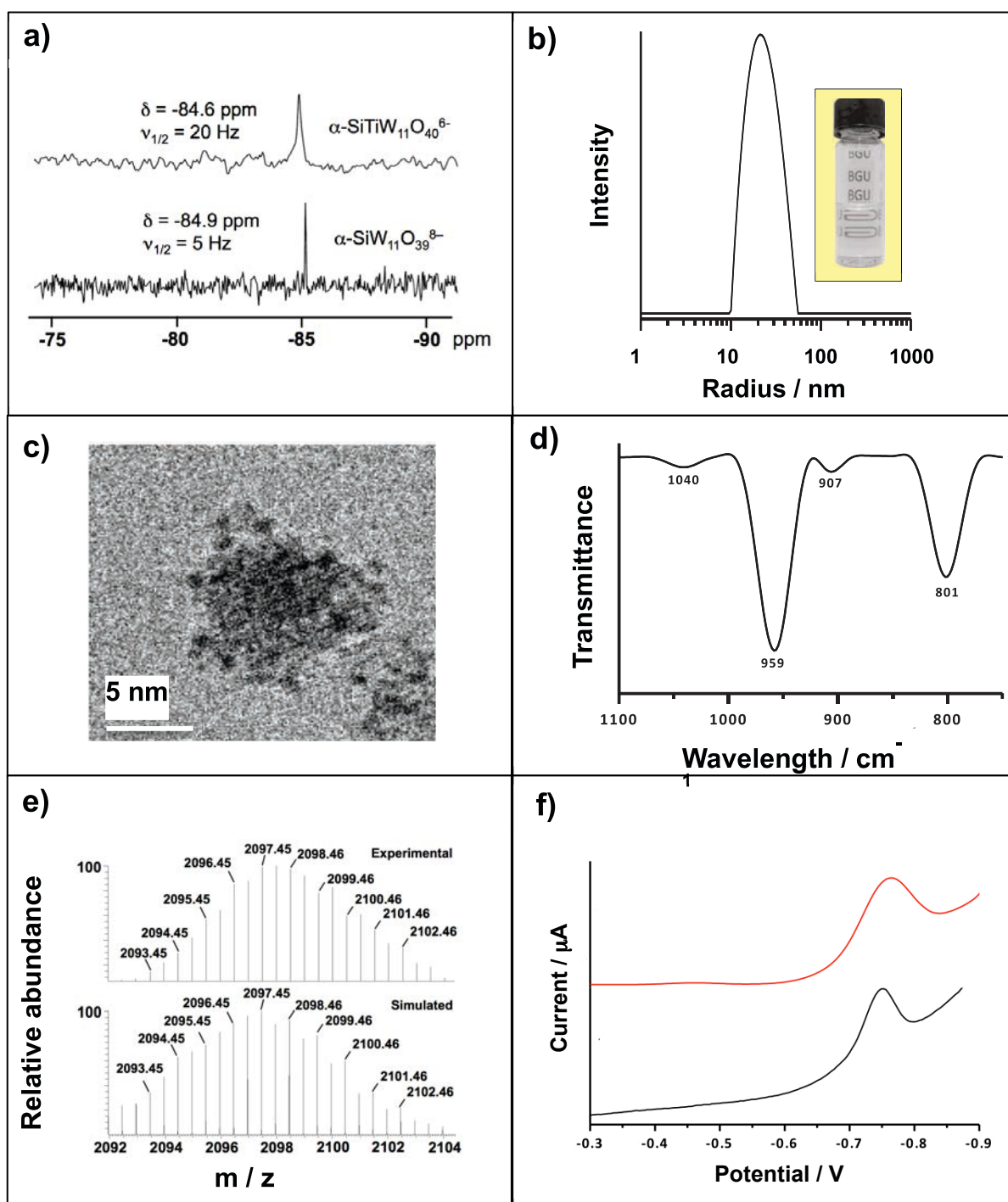


**Figure S14.** Characterization of  $[\alpha\text{-SiW}_{11}\text{O}_{39}\text{Ti}]\text{O}^-$ -capped anatase- $\text{TiO}_2$  nanocrystals. **a)** NMR spectra obtained before (**bottom**) and after (**top**) the reaction of amorphous  $\text{TiO}_2(\text{s})$  with  $\text{K}_8[\alpha\text{-SiW}_{11}\text{O}_{39}]$  for 22 h in water at 170 °C. The signal arising from  $[\alpha\text{-SiW}_{11}\text{O}_{39}]^{8-}$  (pH 6.5) is no longer present, and a new signal at -84.6 ppm (at the final pH of 6.9) is assigned to the Ti(IV) derivative,  $[\alpha\text{-SiTiW}_{11}\text{O}_{40}]^{6-}$ . This may be compared to the  $^{29}\text{Si}$  NMR signal for the  $(n\text{-Bu})_4\text{N}^+$  salt of the proposed *diprotanated* anion,  $[\alpha\text{-H}_2\text{SiTiW}_{11}\text{O}_{40}]^{4-}$  in *DMSO* (not isolated in analytically pure form), which was observed at -84.2.<sup>[14]</sup> In the present case, ESI MS of the solution (after removing the  $\text{TiO}_2$  NCs by nano-filtration, and precipitation of the POM by addition of TBABr) gave a dominant envelope of signals corresponding to the  $\{\text{TBA}_7\text{H}[\alpha\text{-SiTiW}_{11}\text{O}_{40}]\}^{2+}$  ion (see Figure S15). **b)** DLS data showing the ca. 15 nm average hydrodynamic radius ( $R_{\text{hyd}}$ ) of the anatase- $\text{TiO}_2$  NCs in the clear, colorless solution (**inset**) obtained after reaction at 170 °C (a trace of precipitate observed at the bottom of the reaction vessel was removed). For comparison, the  $R_{\text{hyd}}$  of NCs prepared using the  $\text{Na}^+$  salt of  $[\alpha\text{-PW}_{11}\text{O}_{39}]^{7-}$  was ca. 10 nm. **c)** Cryo-TEM image obtained from the clear solution obtained after four cycles of NaCl precipitation, centrifugation, and re-dissolution in pure water. As was true for the  $[\alpha\text{-PW}_{11}\text{O}_{39}\text{Ti}]\text{O}^-$ -capped anatase- $\text{TiO}_2$  NCs, the Si(IV)-heteroatom analog is remarkably resistant to aggregation, and after repeated exposure to large concentrations of NaCl, the 1-nm cluster-anions are clearly observed at the NC surface in the cryo-TEM image of the particle in its vitrified solution state. **d)** FTIR spectrum of dried  $[\alpha\text{-SiW}_{11}\text{O}_{39}\text{Ti}]\text{O}^-$ -capped anatase- $\text{TiO}_2$  NCs, after subtracting the absorbance due to  $\text{TiO}_2$ . As was true for the P(V)-heteroatom analog (Figure S6), the concentration of POM clusters is much smaller than that of  $\text{TiO}_2$  units, the absorption of which increases steeply from 950 to 800  $\text{cm}^{-1}$  (Figure S6, panel **a**). In that case, the baseline correction is *definitively shown* to artificially decrease the relative intensity of the band assigned to the asymmetric W-O-W inter-triad corner-sharing stretch at ca. 900  $\text{cm}^{-1}$  (Figure S6, panel **b**). In the present case (panel **d**), this affect is

more pronounced. With that taken into consideration, the baseline-corrected FTIR spectrum is similar to those of  $K_6[\alpha\text{-SiW}_{11}\text{O}_{39}]$  and  $K_6[\alpha\text{-SiV}^{\text{IV}}\text{W}_{11}\text{O}_{40}]$  (while not identical to either one). **e**) ESI mass spectrum (and the corresponding simulation) obtained after digesting the  $[\alpha\text{-SiW}_{11}\text{O}_{39}\text{Ti}]\text{-O}^-$ -capped anatase- $\text{TiO}_2$  nanocrystals using conc. HCl and then precipitating the *n*-Bu<sub>4</sub>N-salt of the POMs, isolating it as a white solid, and dissolving the solid in acetonitrile. The envelope is centered around a peak (2097.45 amu) that matches the 2+ anion,  $\{\text{TBA}_6\text{H}_2[(\text{SiTiW}_{11}\text{O}_{39})_2\text{O}]\}^{2+}$ . **f**). Differential pulse voltammetry. **Black curve**:  $[\alpha\text{-SiW}_{11}\text{O}_{39}\text{Ti}]\text{-O}^-$ -capped anatase- $\text{TiO}_2$  NCs in 200 mM  $\text{LiClO}_4$  (aq). The DPV was carried out after four cycles of precipitation (2 M NaCl), centrifugation, and re-dissolution of the isolated white material in pure water. As expected, the first reduction wave appears at ca. 175 mV more negative than the corresponding reduction of  $[\alpha\text{-PW}_{11}\text{O}_{39}\text{Ti}]\text{-O}^-$  ligands (see Figure 6b in the text). Due to the large background reduction of water and/or Ti(IV) (i.e.,  $\text{TiO}_2$ ) that commences at ca. -900 mV, the second reduction wave of the  $[\alpha\text{-SiW}_{11}\text{O}_{39}\text{Ti}]\text{-O}^-$  capping ligands is not seen. **Red curve**: For approximate comparison, we provide here the DPV of 0.1 mM  $[\alpha\text{-SiV}^{\text{IV}}\text{W}_{11}\text{O}_{40}]^{6-}$ , an isoelectronic analog of  $[\alpha\text{-SiTi}^{\text{IV}}\text{W}_{11}\text{O}_{40}]^{6-}$ ; conditions: pH 5.7 in 200 mM  $\text{LiClO}_4$  and 70 mM acetate buffer.

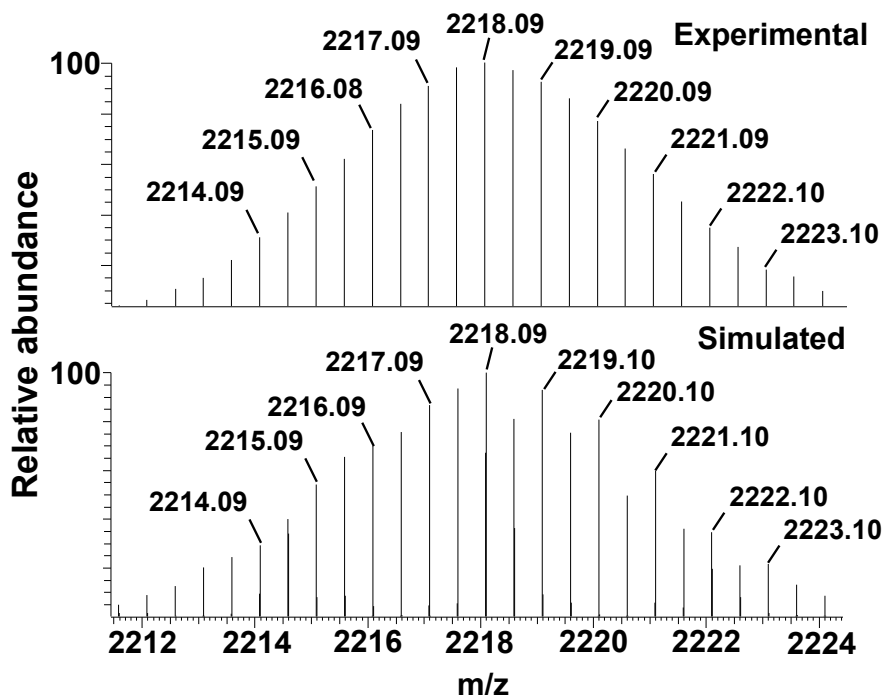


**Figure S15.** ESI mass spectrum of the TBA salt of the Ti-containing byproduct,  $[\alpha\text{-SiTiW}_{11}\text{O}_{40}]^{6-}$ , formed during synthesis of the  $[\alpha\text{-SiW}_{11}\text{O}_{39}\text{Ti}]\text{-O}^-$ -capped anatase- $\text{TiO}_2$  NCs. The experimental and simulated spectra are effectively identical. This supports assignment of the new  $^{29}\text{Si}$  NMR signal in Figure S14a (**top**) to  $\alpha\text{-SiTiW}_{11}\text{O}_{40}]^{6-}$ . The observed envelope corresponds to that of the  $z = 2+$  ion,  $\{\text{TBA}_6\text{H}[(\text{SiTiW}_{11}\text{O}_{40})_2]\}^{2+}$ .

## Discussion [added in revision]: Comparison of the spectroscopic and electrochemical properties of the POM ligands in $[\alpha\text{-PW}_{11}\text{O}_{39}\text{Ti}]\text{-O}^-$ -bound anatase- $\text{TiO}_2$ NCs with those of other Ti-substituted heteropolytungstates.

Comparison of the spectroscopic and electrochemical properties of the  $\text{PTiW}_{11}\text{O}_{40}^{5-}$ -derived POM ligands on  $\text{TiO}_2$  (labelled, **2'**) with those of  $\text{PTiW}_{11}\text{O}_{40}^{5-}$  (**2**) are included in the original version of the manuscript. Namely, respective IR spectra are compared in Figure 4 of the text, CV data (in our case, differential pulse voltammetric, DPV, data) are compared in Figure S13, and MAS P NMR data are compared in Figure S7. In addition, the small difference in chemical shift values between the monomeric and dimeric forms of  $\text{PTiW}_{11}\text{O}_{40}^{5-}$  (**2**) are discussed in Figure S8.

These data should first be compared with corresponding data obtained for the monomeric and dimeric forms of the mono-titanium-substituted  $\alpha_2$  derivative of the Wells-Dawson anion, i.e.,  $[\alpha_2\text{-P}_2\text{W}_{17}\text{TiO}_{62}]^{8-}$  and  $[(\alpha_2\text{-P}_2\text{W}_{17}\text{TiO}_{61})_2(\mu\text{-O})]^{14-}$ .  $^{31}\text{P}$  NMR spectra (in  $\text{D}_2\text{O}$ , with 85% phosphoric acid set to 0 ppm), revealed two signals each (as expected for Wells-Dawson structures), at -10.1 and -13.7 ppm for the monomeric form, and -10.7 and -13.5 ppm for the dimer. By comparison, the  $^{31}\text{P}$  NMR spectra of **2** contain only one signal, as expected for derivatives of the Keggin structure. Due to the significant differences in numbers and types of bridging- and corner-sharing oxide linkages between W atoms in the Wells-Dawson versus Keggin structures, the FTIR spectra of both  $[\alpha_2\text{-P}_2\text{W}_{17}\text{TiO}_{62}]^{8-}$  and  $[(\alpha_2\text{-P}_2\text{W}_{17}\text{TiO}_{61})_2(\mu\text{-O})]^{14-}$  are distinctly different from those of **2** and **2'**. (This is readily apparent by visual comparison of Figure 1 from page 4632 of ref. [15] with the spectra in Figure 4 of the text (this work)). The MAS  $^{31}\text{P}$  spectra of both the monomeric and dimeric forms of the Wells-Dawson derivatives show broad signals near -14 and -11 ppm, while the MAS  $^{31}\text{P}$  spectrum of **2** (this work; Figure S7) contains two signals (very close to one another) near -15 ppm, but no signals at smaller ppm values. The MAS  $^{31}\text{P}$  spectrum of **2'** contains a much broader signal, as is typical for solid-state NMR spectra of POM ligands bound to nanoparticles and surfaces (see the caption to Figure S7 for discussion and citations to that literature). To our knowledge, electrochemical data for the above-noted titanium-substituted Wells-Dawson compounds have not been reported. However, differential pulse voltammetry data for  $[\alpha_2\text{-P}_2\text{W}_{17}\text{V}^{\text{IV}}\text{O}_{62}]^{8-}$ , an isostructural and isoelectronic analog of  $[\alpha_2\text{-P}_2\text{W}_{17}\text{Ti}^{\text{IV}}\text{O}_{62}]^{8-}$ , is sequentially reduced, with cathodic maxima at 477, 716 and 905 mV (versus Ag/AgCl in 3 M NaCl). These values are quite distinct from those observed for **2'**, for which,



cathodic maxima are located at -565 and -790 mV (Figure 6b in the text). These data definitively rule out the presence of Wells-Dawson-anion derivatives at the surfaces of the TiO<sub>2</sub> nanocrystals (NCs). The same is true for other titanium-substituted derivatives of the Wells-Dawson anions (see articles cited in the introduction to ref. [16]), whose spectroscopic properties differ markedly from those of Keggin ions such as **2** and **2'**.

The di-titanium substituted mixed-addendum Keggin heteropolytungstophosphate (and their dimeric forms),<sup>[17]</sup> are logically the next type of Ti-containing POM that might be compared with **2'**. For the di-titanium compounds (monomeric [ $\alpha$ -1,2-PW<sub>10</sub>Ti<sub>2</sub>O<sub>40</sub>]<sup>7-</sup> and dimeric [ $\alpha$ , $\alpha$ -P<sub>2</sub>W<sub>20</sub>Ti<sub>4</sub>O<sub>78</sub>]<sup>10-</sup>), <sup>31</sup>P NMR chemical shifts (in D<sub>2</sub>O, relative to 25% phosphoric acid set to 0 ppm) are observed at -12.14 and -11.74 ppm, respectively. Both of these values are distinct from the chemical-shift values observed in the present work for **2** (-13.90 ppm), and its dimeric form present at pH values below 0.6, for which the <sup>31</sup>P NMR signal appears at -13.96 ppm (see Figure S8). The FTIR spectra of monomeric [ $\alpha$ -1,2-PW<sub>10</sub>Ti<sub>2</sub>O<sub>40</sub>]<sup>7-</sup> (KBr pellet) contains bands at 1084m, 1062m, 962m, 891m, 818s, 721m, 624m, 480m cm<sup>-1</sup>, while for **2'**, bands appear at 1085, 1066, 960, 880, 820 (no bands between 700 and 800). The spectrum of **2** is very similar, with bands appearing 1085, 1066, 970, 900, 800 (here also, there is no bands between 700 and 800). In short, both **2** and **2'** differ in the energy of the band in the vicinity of 890-900 (arising from the corner-shared, inter-triad W- $\mu_2$ -O-W stretching mode), and unlike the monomeric form of the di-titanium compound, no bands are observed between 700 and 800 cm<sup>-1</sup> for either **2** or **2'**. Even more significant differences are observed when comparing FTIR spectra of **2** and **2'** to that of the dimeric form of the di-titanium-substituted compound, [ $\alpha$ , $\alpha$ -P<sub>2</sub>W<sub>20</sub>Ti<sub>4</sub>O<sub>78</sub>]<sup>10-</sup>, for which, bands are observed at 1065s, 964s, 891m, 798vs, 721s, 593m, 519m, 487m cm<sup>-1</sup>. Notably, no band is observed at energies larger than 1065 cm<sup>-1</sup>. To our knowledge, no CV data are reported for the monomeric or dimeric forms of the di-titanium substituted Keggin phosphotungstate anions. Nevertheless, the available data summarized here definitively rule out the presence of di-titanium substituted Keggin phosphotungstate derivatives at the surfaces of the TiO<sub>2</sub> NCs.

Next, **2** and **2'** are compared with published spectroscopic and electrochemical data for the dimeric form of the tri-substituted Keggin phosphotungstate anion, [ $\alpha$ , $\alpha$ -P<sub>2</sub>W<sub>18</sub>Ti<sub>6</sub>O<sub>77</sub>]<sup>12-</sup>.<sup>[16]</sup> The <sup>31</sup>P NMR spectrum of that dimer (in D<sub>2</sub>O, 85% phosphate set to 0 ppm) appears at -10.49, significantly different from the -13.9 value observed for **2**. Also, the FTIR spectrum of the {P<sub>2</sub>W<sub>18</sub>Ti<sub>6</sub>} dimer, with bands at 1061s, 960s, 889m, 799vs, 731s, 593m, and 519 cm<sup>-1</sup>, is very different from those observed for **2** or **2'**. Although to our knowledge electrochemical data or solid-state MAS <sup>31</sup>P spectra have not been reported for dimeric {P<sub>2</sub>W<sub>18</sub>Ti<sub>6</sub>}, it is clear that the POM ligands observed the surface of the TiO<sub>2</sub> NCs are not tri-titanium substituted Keggin phosphotungstate anions.

Spectroscopic and electrochemical data for other POMs, both with and without titanium addendum atoms, are generally less similar to **2** and **2'** than are the compounds discussed above. From this short overview of available data for the above series of titanium-substituted phosphotungstates, it thus abundantly clear that the POM observed on the TiO<sub>2</sub> NCs, and characterized by ESI-MS, FTIR, UV-vis and <sup>31</sup>P NMR spectroscopy, and voltammetry (DPV), are the {PTiW<sub>11</sub>} anions, **2'**.

## References

- [1] N. Haraguchi, Y. Okaue, T. Isobe, Y. Matsuda, *Inorg. Chem.* **1994**, *33*, 1015-1020.
- [2] C. Tourné, G. Tourné, *Bull. Soc. Chim. Fr.* **1969**, *4*, 1124-1136.
- [3] G. Maksimov, R. Maksimovskaya, O. Kholdeeva, M. Fedotov, V. Zaikovskii, V. Vasil'ev, S. Arzumanov, *J. Struct. Chem.* **2009**, *50*, 618-627.
- [4] A. Tézé, G. Hervé, R. G. Finke, D. K. Lyon, in *Inorganic Syntheses*, Vol. 27 (Ed.: A. P. Ginsberg), John Wiley & Sons, Inc., USA, **1990**, pp. 85.
- [5] I. A. Weinstock, J. J. Cowan, E. M. G. Barbuzzi, H. Zeng, C. L. Hill, *J. Am. Chem. Soc.* **1999**, *121*, 4608-4617.
- [6] Y. V. Geletii, C. L. Hill, A. J. Bailey, K. I. Hardcastle, R. H. Atalla, I. A. Weinstock, *Inorg. Chem.* **2005**, *44*, 8955-8966.
- [7] B.-J. van Rossum, C. P. de Groot, V. Ladizhansky, S. Vega, H. J. M. de Groot, *J. Am. Chem. Soc.* **2000**, *122*, 3465-3472.
- [8] L. G. Detusheva, M. A. Fedotav, L. L. Kuznetsova, A. A. Vlasov, G. A. Likholobov, *Russ. Chem. Bull.* **1997**, *46*, 874-880.
- [9] G. M. Maksimov, L. I. Kuznetsova, K. I. Matveev, R. I. Maksimovskaya, *Koord. Khim.* **1985**, *11*, 1353-1357.
- [10] Y. Mao, S. S. Wong, *J. Am. Chem. Soc.* **2006**, *128*, 8217-8226.
- [11] J. C. Edwards, C. Y. Thiel, B. Benac, J. Knifton, *Catal. Lett.* **1998**, *51*, 77-83.
- [12] T.-h. Chang, *J. Chem. Soc., Faraday Trans.* **1995**, *91*, 375-379.
- [13] S. Uchida, K. Inumaru, M. Misono, *J. Phys. Chem. B* **2000**, *104*, 8108-8115.
- [14] Y. Goto, K. Kamata, K. Yamaguchi, K. Uehara, S. Hikichi, N. Mizuno, *Inorg. Chem.* **2006**, *45*, 2347-2356.
- [15] S. Yoshida, H. Murakami, Y. Sakai, K. Nomiya, *Dalton Trans.* **2008**, 4630-4638.
- [16] K. Nomiya, M. Takahashi, K. Ohsawa, J. A. Widegren, *J. Chem. Soc., Dalton Trans.* **2001**, 2872-2878.
- [17] K. Nomiya, M. Takahashi, J. A. Widegren, T. Aizawa, Y. Sakai, N. C. Kasuga, *J. Chem. Soc., Dalton Trans.* **2002**, 3679-3685.